

# **Chapter 7 Appendix II. Fourier-transform spectrometer for solar occultation mission of wide spectral range**

- A compact space-borne FTS of moderate spatial and spectral resolution -

The instrument described in this chapter is a solar occultation Fourier Transform Spectrometer (FTS), which will be placed in a 650 km non-sun-synchronous orbit, with an inclination angle of 69 deg. It is the successor of ILAS-II, which will be onboard the Advanced Earth Observing Satellite-II (ADEOS-II). It measures atmospheric constituent vertical profiles with  $0.24 \text{ cm}^{-1}$  spectral resolution in 3-13  $\mu\text{m}$  and 1 km vertical resolution. It will measure the global distribution of  $\text{O}_3$ ,  $\text{HNO}_3$ ,  $\text{NO}_2$ ,  $\text{N}_2\text{O}$ ,  $\text{CH}_4$ ,  $\text{H}_2\text{O}$ ,  $\text{CO}_2$ , CFC-11, CFC-12,  $\text{ClONO}_2$ , aerosol extinction, atmospheric pressure, and temperature. Main objective is to provide the global data to constrain the uncertainty of the source and sink retrieval of the green house gases. The instrument uses a double-pass dual-pendulum type FTS with diode laser sampling system to reduce the size and weight. Two photo-voltaic (PV) MCT (HgCdTe) detectors and a pulse-tube cooler will achieve high linearity and low-noise performance. In addition, it has a visible ( $\text{O}_2 A$  band) grating spectrometer for pressure and temperature retrieval and a sun-edge sensor for the tangent height position detection. The performance test results of the laboratory model are described and the instrumentation and engineering model test results are presented.<sup>1</sup>

---

<sup>1</sup> This chapter has been published in "Conceptual Design of Solar Occultation FTS for Incline-orbit Satellite on GCOM-A1," SPIE 4131, 305-314, (2000) and "Instrumentation and laboratory model test result of Solar Occultation FTS for Inclined-orbit Satellite (SOFIS) on GCOM-A1," SPIE 4486, 356-365, (2002) and were co-authored by Y. Sasano, H. Nakajima, and J. Tanii. They were updated and revised.

## 7.1. Scientific Objectives

The instrument discussed here is a solar occultation FTS which will be placed in a 650 km non-sun-synchronous orbit, with a 69 degrees inclination [M. Suzuki *et al.*, 2000]. IR Solar occultation is a comprehensive method to monitor the green house gases. Regional emission source will be retrieved by comparing the acquired global data and the chemical transport model [Gurney *et al.*, 2002 and Pak *et al.*, 2001]. It will provide global data especially in tropical region, and vertical profile data, which are not available from the existing ground stations. It is designed as a successor of ILAS and ILAS-II [M. Suzuki *et al.*, 1994, Sasano *et al.*, 1999, and M. Suzuki *et al.*, 1995]. The spectral resolution will be improved by replacing the grating spectrometer by the FTS and the pyroelectric detector by the cooled PV-MCT detector. The laboratory model of the PV-MCT detector has been manufactured and the conceptual study has been completed. The scientific objectives, mission concept, conceptual design of the instrument, the detailed specifications and configuration of the components were presented in the former study [Kuze *et al.*, 2000 and H. Nakajima *et al.*, 2001]. The sensitivity was studied to specify the wavelength region, spectral resolution, and signal-to-noise ratio (SNR) requirements [Uemura *et al.*, 2001]. The performance of the single-side and both-side scans and the effect of the tangent height change during the interferogram acquisition were also numerically simulated and traded off. The result shows that the interferogram acquired with the both-side scan includes both low and high altitude data at the maximum path difference, in other words, high frequency information in the spectral domain. As a consequence, the inverse Fourier transferred spectra will minimize the artificial oscillation and provide a smooth vertical profile. In addition, the both-side scan will correct the phase delay properly. In this chapter, the design updates, the instrumentation, the key technologies to achieve the required performance, and the operation in orbit are described. To reduce the development risk and to validate the key performances, a laboratory model has been manufactured and test data has been acquired.

## 7.2. Requirements and Design Concept

**Occultation measurement and calibration.** One advantage of the solar occultation technique is the high radiance of the light source, which enables high spectral resolution measurement with high SNR. Another advantage is that full and zero levels can be calibrated during the same occultation measurement through the earth's atmosphere as shown in Figure 7-1. The target altitude range of the measurement is from 5 km to 120 km in the case without high tropospheric clouds.

**Spectral coverage.** The spectral range is designed to include both the ILAS and ILAS-II coverage for continuity. Figure 7-2 shows the simulated absorption spectra of the infrared region with MODTRAN version 3 [Berk *et al.*, 1989]. To minimize the non-linearity effect, the optical bandwidth of the spectral band is less than one octave. Therefore the FTS has two spectral bands: 3.25-6.5  $\mu\text{m}$  and 6.5-13  $\mu\text{m}$ , as shown in Figure 7-3. The spectral range is selected to cover both  $\text{ClONO}_2$  (12.8  $\mu\text{m}$ ) and HCl (3.5  $\mu\text{m}$ ) absorption spectra.

**Height resolution and spectral resolution.** Sensitivity study has shown that a resolution higher than 0.2  $\text{cm}^{-1}$  is required for HCl and  $\text{ClONO}_2$  retrieval. Thus a spectrometer with 0.2  $\text{cm}^{-1}$  resolution has enough sensitivity not only to retrieve the major and key atmospheric constituents, but also to increase the opportunity to

measure the absorption spectra of moderate optical thickness.

From an engineering point of view, the FTS with  $0.2 \text{ cm}^{-1}$  resolution and SNR better than 300 requires at least 16 digitizing bits. However, the speed of a 16 bit AD converter limits the sampling frequency. The current design of the instrument will acquire an interferogram for every 1.2 km in height with 1.1 km resolution. As the tangent height changes at a rate of 3.17 km/sec (the fastest case), the instrument has to acquire an interferogram every less than 0.372 sec. Because the tangent point changes with the satellite motion, the DC levels during one interferogram acquisition also change. However, in the retrieval, the error due to this change is negligibly small.

**Global coverage.** The satellite orbit has been selected for the instrument to measure from the equator to high latitudes. Its orbit is non-sun-synchronous and its inclination angle and altitude are optimized for global coverage. Figure 7-4 shows the latitudinal coverage assuming a launch on January 1 at 8:00 am.

**Temperature and pressure retrieval.** To retrieve gas data from solar occultation measurements, it is essential to determine the temperature and pressure of the tangent airmass. The  $\text{O}_2 A$  band spectra will be used for temperature and pressure retrievals. This method has been applied to both ILAS and ILAS-II.

**Solar image and IFOV position.** The sun edge position and the instantaneous field of view (IFOV) position data are detected with a linear array detector to determine the observation geometry. One solar image (radiance distribution) is also acquired per occultation event to detect the locations of sunspots.

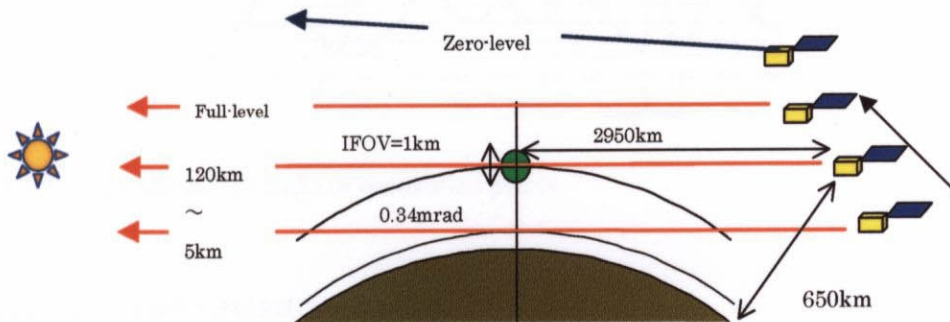


Figure 7-1. Mission concept of the solar occultation.

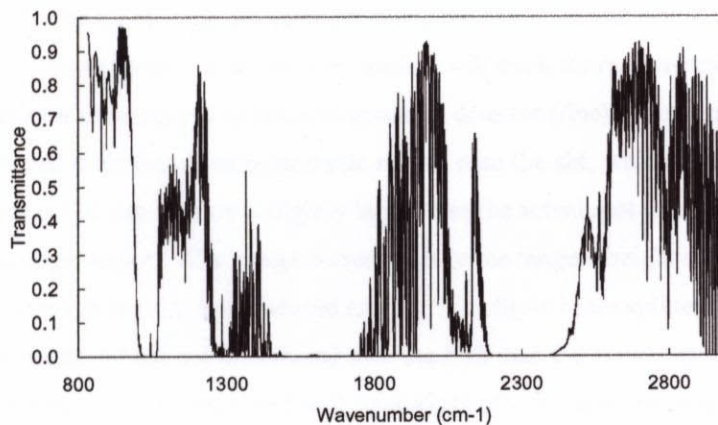


Figure 7-2. Absorption spectra in the case of looking at the tangent point of 10 km calculated with MODTRAN.

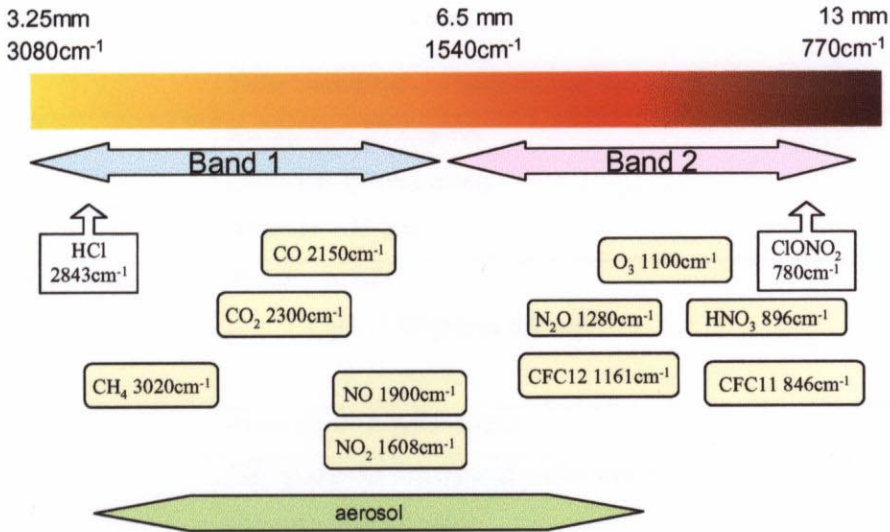


Figure 7-3. The spectral coverage and target species.

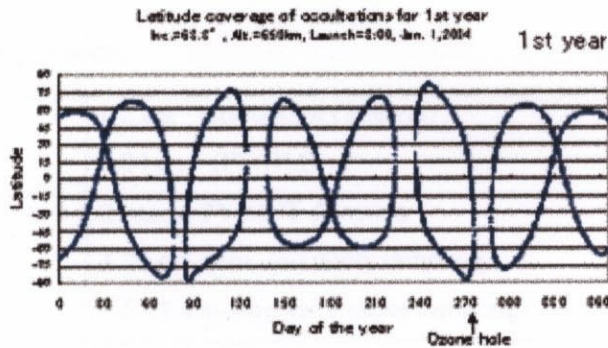


Figure 7-4. Latitudinal coverage of occultation points.

### 7.3. Specification and Instrumentation

The instrument consists of a sun tracking gimbal, relay optics, Fourier transform spectrometer (FTS), visible spectrometer, sun edge sensor, and their related electronics. The specifications and its FTS are described in Table 7-1 and Table 7-2. Its block diagram, configuration, and optical layout are summarized in Figure 7-5, Figure 7-6, and Figure 7-7, respectively. The two-axes gimbal will track the radiometric center of the sun with a Si position sensitive detector (coarse) and an InGaAs quadrant detector (fine) at both sunrise and sunset. The tracked solar flux is collected with the off-axis parabolic mirror onto the slit, which has a mirror surface. The diameter of the circular slit is  $110 \mu\text{m}$ , which is slightly larger than the actual spot size. The reflected slit image is monitored with the sun edge sensor. The image corresponds to the tangent height of 1.1 km (FWHM). The scene flux, which passes through the slit, is collimated again. A dichroic beam splitter divides the flux into the infrared (IR) and visible bands, which are introduced into the FTS and the visible spectrometer, respectively. The transmitted IR flux enters the FTS optics and will be modulated. An aperture stop of the optics is placed between the FTS and the band separation optics. The field stop is the FTS detector itself.

Table 7-1. Specifications of the instrument.

Method	Solar occultation of both sunrise and sunset
Satellite Orbit	Inclination: 69 degrees (Non-sun synchronous) Altitude: 650 km
IFOV (instantaneous field of view)	Tangent height: 1.1 km (FWHM) at 6.5 $\mu\text{m}$ 0.7 km (interval)
FOV	From 5 km to outer space
Calibration	Full level: the sun through outer space Zero level: deep space
Sun tracking	Radiometric center tracking with two-axes gimbal

Table 7-2. The FTS summary.

Spectral resolution	0.2 $\text{cm}^{-1}$ unapodized (interval) 0.24 $\text{cm}^{-1}$ (FWHM)
Wavelength region	2 bands, PV-MCT detectors 3.25-6.5 $\mu\text{m}$ (no under sampling) 6.5-13 $\mu\text{m}$ (interval 2 under sampling)
Interferogram scan	0.23 sec per interferogram Both-sides, both-ways
Zero path difference detection	White light
Scan direction detection	Two polarized phase shifted diode lasers and Si-detectors
Scan speed stability	+/-1% rms with servo control
SNR	More than 300 with 16-bit ADC
Sampling reference	Diode laser of 1550 nm InGa pin diode detector
Beam splitter and compensator	ZnSe
FTS type	Double corner cubes, double path

The instrument is designed to provide wide spectral-range data to monitor the major greenhouse gases using the FTS technique. The FTS has a moderate resolution (0.24  $\text{cm}^{-1}$ ) and the quick scan enables us to carry out high vertical resolution measurements. The FTS will acquire the interferogram every 0.23 sec. Thus it can sample at an altitude interval of less than 0.7 km with 1.1 km IFOV. It has double-corner-cube type interferometer with a flexible blade as shown in Figure 7-8. The optical path is doubled by inserting a reflecting mirror inside the FTS. The modulated flux is divided into two spectral bands in the after optics with the dichroic beam splitter and the band pass filter. To minimize the non-linearity effect, the spectral bandwidth is

designed to be less than one octave. The modulated flux is collected on the dewar focal plane, where the two MCT detectors are mounted.

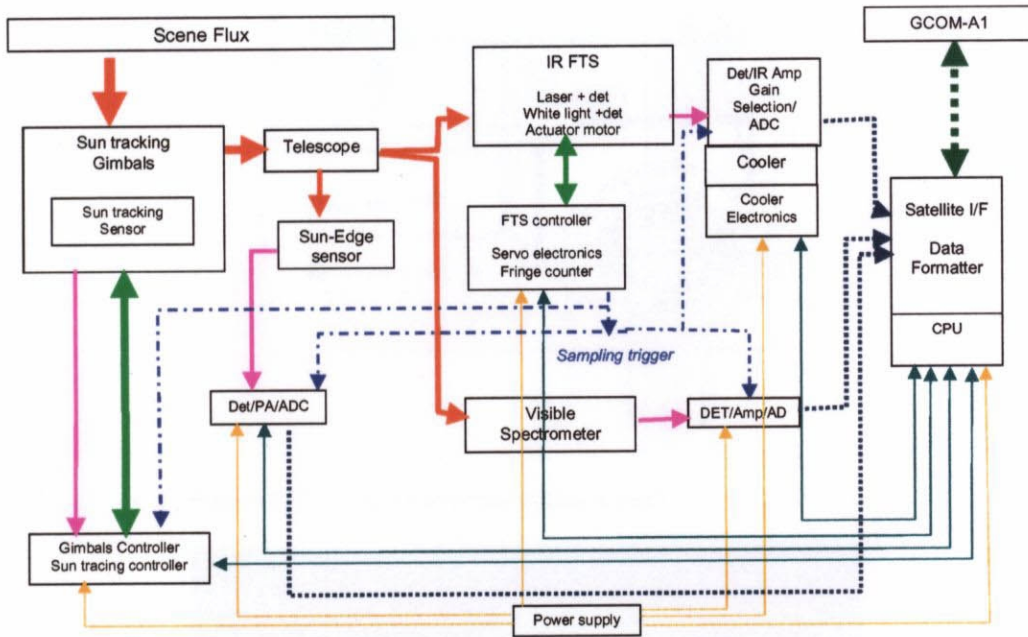


Figure 7-5. The instrument function diagram.

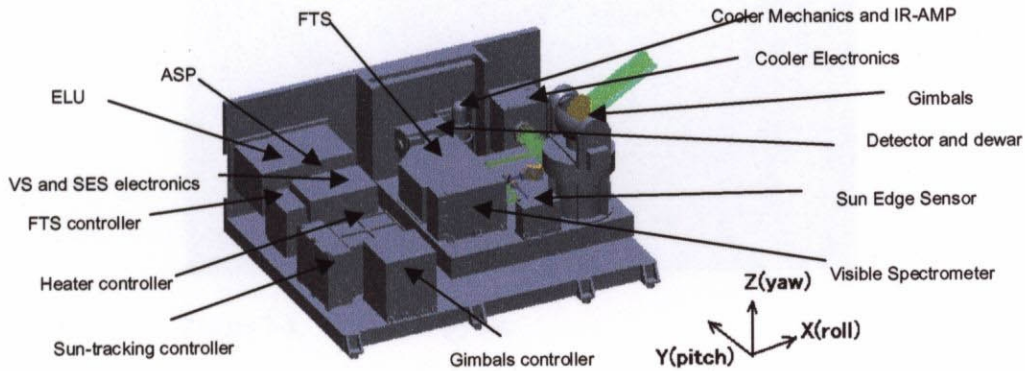


Figure 7-6. The instrument configuration.

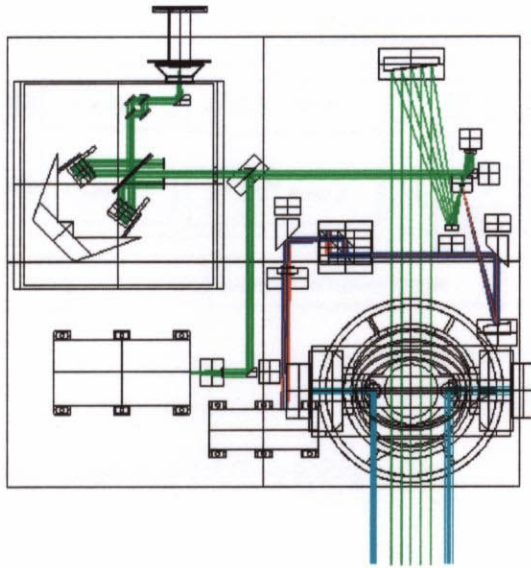


Figure 7-7. The instrument optics layout.

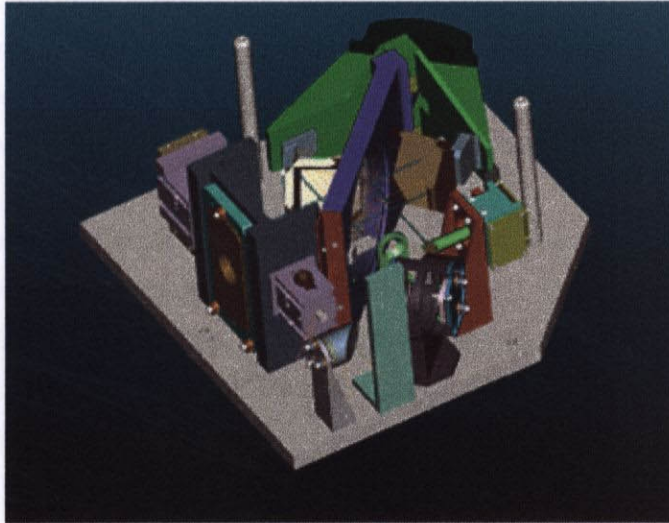


Figure 7-8. The FTS layout.

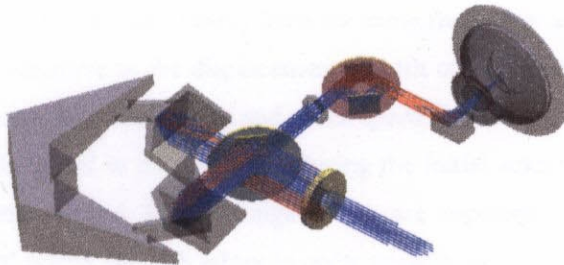


Figure 7-9. FTS, band separation and detector optics layout.

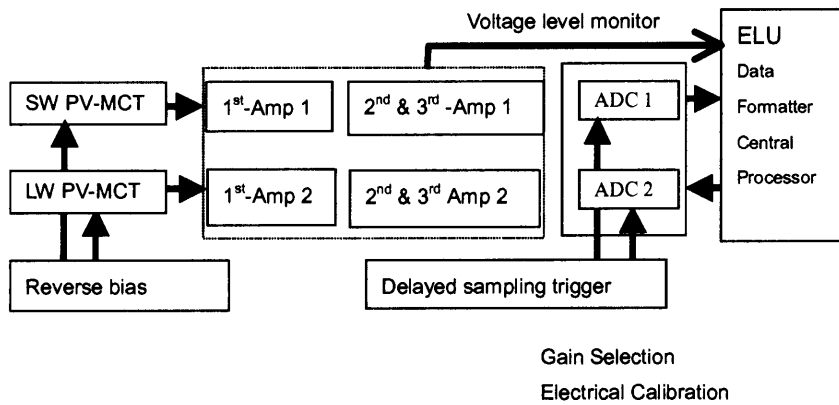


Figure 7-10. Block diagram of the IR sampling system.

**Sun-tracking with two-axes gimbals.** The fine and coarse sun sensors, which are mounted on the two-axes gimbals, will detect the radiometric center of the sun. The higher speed sun sensor sampling and the higher frequency servo control will enable more stable tracking and can start the tracking from lower altitude (upper troposphere) at sunrise. As the satellite size is medium, the instrument can be disturbed by the thermal snap of the solar paddle at the sunrise. To overcome this disturbance, the gimbals have a feed forward control system and the satellite will provide its gyro data to the gimbals controller, directly. Thus the instrument can track the sun precisely.

**Visible spectrometer and sun edge sensor.** Accurate height detection is one of the most important performances of the solar occultation measurements. The combination of the visible spectrometer and the sun edge sensor will determine IFOV and retrieve the temperature and pressure of certain tangent height. Table 7-3 and Table 7-4 show their specifications. The visible spectrometer will measure the bandwidth and strength of the  $O_2 A$  band absorption spectra. The slit position is ray traced and the height is retrieved from the upper edge of the solar image. The visible spectrometer will transmit 5 datasets per interferogram and the sun edge sensor will provide 2 datasets. These more frequent data acquisitions than the interferogram will ensure the smooth height retrieval.

**FTS.** To maximize the modulation efficiency, the flat mirror doubles the optical path difference and compensates the misalignment. The divided beams share the same flat mirror as shown in Figure 7-9. In this configuration, the FTS is less sensitive to the displacement and tilt of the optical components. To achieve a uniform scan speed, feed forward control is applied and so the speed fluctuation will be less than 1%. The FTS controller has the servo profile stored in its memory. During the initial scan with white light, the zero path difference (ZPD) point is detected and 32,458 fringe points are registered in both sides of ZPD. This gated-window has an extra 100 points for both edges in order to calibrate the ZPD on the ground. The beam splitter and the compensator are wedged to avoid the channeling effect.

**IR Detector, dewar, amplifier, and sampling system.** The two PV-MCT detectors are mounted on the dewar, which is connected to the cooler head and cooled to 70 K. The dewar is electrically isolated from the cooler with a sapphire rod. The sapphire rod is connected to the 65 K cold head with a metal coupler, which absorbs the displacement between the cooler and the dewar. The dewar has a Ge window, which is tilted and

wedged. The tilted window prevents the modulated light from reentering the FTS. The wedged window avoids the channeling effect. For the FTS application, the non-linearity and phase delay must be corrected. By minimizing the error caused by these corrections, FTS will provide high fidelity interferograms. PV-MCT detectors have essentially higher linearity than PC-MCT. The detectors are reverse-biased to produce high impedance and match the amplifier. Figure 7-10 shows the block diagram of the IR sampling system. The three stage amplifiers are mounted closed to the detector. The Bessel filter of the amplifier has a flat time delay over the target frequency, in other words, over the target spectral region. To the analogue-to-digital converters (ADC), the FTS controller will provide delayed sampling triggers, which compensate the delay caused by the amplifier. Thus the non-linearity and the phase delay of the interferogram are very small.

**Temperature control and its stability on orbit.** To minimize the thermal distortion on orbit, all the optical components are mounted on an optical bench, which is made of a carbon fiber reinforced plastic (CFRP). The related electronics are mounted on the base plate and side panel. The optical bench is mounted with three kinematic mounts, which release the distortion between the outer structure and the optical bench. The FTS optics base, which is made of aluminum, is also attached to the optical bench with three kinematic mounts. The temperature of the optical bench is controlled to 23+/- 3 degrees C, at which the instrument will be integrated on the ground. The major heat sources on the optical bench are the gimbal motor and the sampling laser of the FTS. The gimbals are thermally isolated with a CFRP pedestal. The temperature of the laser is set by commands on orbit for the wavelength stability and minimizing power consumption. The heat of the laser temperature controller is dissipated from the FTS cover by radiative cooling. In addition, the instrument has a multi channel digital heater controller. The temperature of the components and the optical bench can be set and controlled by commands. The cooler and the electronics unit (ELU) are the major heat sources and they are mounted on the side panel, which is always viewing deep space. Thus the temperature potential of the optics is cooled down and the optical bench is always heater-controlled to stabilize the temperature.

**Gain tuning capability.** For the solar occultation application, the gain level is designed such that the full solar signal level looking through outer space is the maximum level of the dynamic range. However, there exist some uncertainties caused by mis-alignment, thermal distortion, sag due to gravity release, and degradation during the mission. To adjust the dynamic range properly, two methods will be applied; one is gain tuning of the amplifier during the integration on the ground and the other is gain selection of the amplifier on orbit by commands.

Table 7-3. Sun edge sensor summary.

Image	Reflected slit image
Detector	5000-pixel Si-CCD
A/D bit	12 bits
Sun edge detection	Two images per interferogram
Solar image	Solar disk scan with gimbal elevation motion

Table 7-4. Visible spectrometer summary.

Spectral range	753-784 nm
Spectral resolution	0.06 nm
Optics	Reflective (telecentric)
Grating	1800 grooves/mm, holographic
Detector	1024-pixel Si-CMOS
Data acquisition	5 datasets per interferogram
A/D bit	16 bits

## 7.4. Operation

To meet the long-term monitoring purposes, the instrument will be operated to provide accurate data continuously with high fidelity. To achieve robustness, contamination rejection, and reliability, special care has been taken of operation. The ELU controls the gimbals, the FTS, the cooler, the visible spectrometer, the sun edge sensor and their operation sequence. It has two central processor units (CPU). The ELU will receive the observed data and the house keeping telemetries from the components and edit them with the CCSDS packet format. It will then transmit the data to the satellite as science data where they are stored in the data recorder of the satellite until it passes over the ground station.

**Occultation event operation sequence.** During the normal operation, there are two modes: standby and observation modes. The sampling laser and the cooler are always turned on for their stabilization. In the standby mode, the gimbals mirror points inside the protection cover to prevent contamination, then prior to the occultation measurement, the gimbals flip to the expected solar direction for quick tracking. This waiting position will be updated periodically by transmitting the angle data by commands. As the satellite orbit is non-sun synchronous, the sun angle (beta angle) varies. Frequent and accurate updating will enable lower altitude (troposphere) measurement at sunrise events. Figure 7-11 shows the operation sequence. By using the white lamp, the fringe counter of the FTS is updated at the beginning of every observation mode. Before and after the occultation event, the gimbals point towards deep space for zero level calibration. In addition, the gimbals view the solar disk through outer space to calibrate the full level and then scan the solar disk vertically to detect the distribution of sunspots. The number of interferograms, datasets, and their related telemetries are counted by the ELU, which transmits a uniform amount of data in each occultation event.

**Science dataset.** All the data needed for the data processing and data correction are transmitted to the ground as science data. The contents of the mission data are described in Table 7-5. The laser sampling system will provide the every 1.55  $\mu\text{m}$  optical path difference fringe. The FTS controller will count fringes from the turn around. The FTS is the only component that has mechanical parts. The data transmission timing is based on the FTS mechanics motion. The FTS controller will provide the gated sampling triggers for the ADCs of the IR detectors. It also will provide the gimbals, visible spectrometer, and sun edge sensor with the turn around signal. Thus the visible spectrometer, gimbals status data and sun edge sensor data are synchronized with the turn around signal. Each dataset has a time stamp in its header and will be identified with

the GPS time (the satellite time). The FTS telemetries include the FTS actuator scan speed (10 points per interferogram), its scan direction, and the laser diode temperature. The cooler telemetries are the piston frequency, cold head temperature, and other parameters. In addition, the temperature of each component is monitored as the house keeping telemetry.

**Wavelength calibration.** Before launch, the instrument functions will be measured at several wavenumbers with a tunable diode laser. The shape is assumed not to be changed on orbit. During the mission on orbit, the absolute central wavelength will be calibrated using the line absorption database of the atmospheric constituents.

**Radiometric and electric calibration.** The advantage of the solar occultation method is the self-calibration capability. By viewing deep space and tracking the sun through outer space, both zero and full levels are calibrated within one occultation event. In addition, the reference voltage is provided directly to the ADCs of each spectrometer for the electric calibration.

**Cooler diagnostics.** The condition of the cooler will be checked in the diagnostics mode. During the diagnostics mode, the cooler controller transmits the detailed telemetry such as cold head temperature and vibration control.

**Redundancy.** As the FTS is the most important component, redundancy and fail-safe design have to be considered. It has a redundant white light and diode laser. In addition, in case of failure of the white light, it can detect the zero path difference with an optical switch, which is attached to the edge of the FTS actuator. In case of the laser failure, the FTS controller will use the scan profile for the actuator control (open loop control). The selection of the white lamp and the laser is controlled by commands.

**De-contamination.** Once the response of the IR signal has degraded and it is assumed to be due to contamination on the cold surface, the cooler will be turned off. The cooler head and the dewar temperature will be kept at the surrounding temperature for a certain duration to evaporate the contamination.

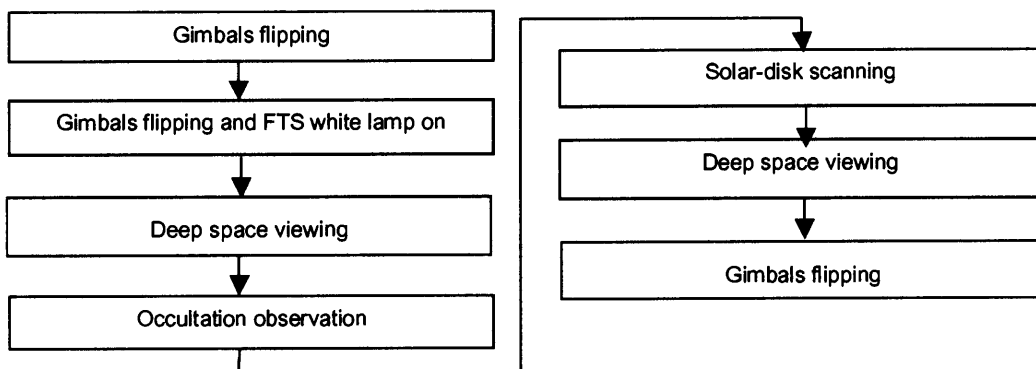


Figure 7-11. The operation sequence (sunrise).

Table 7-5. List of the science data.

Raw interferogram (2 bands)
O <sub>2</sub> A band spectra, 5 datasets per interferogram
Sun edge sensor data, 2 datasets per interferogram
FTS, cooler, detector, and gimbals house keeping data

## 7.5. Key Technology and Laboratory Test Results

For the development, we will make full use of the ILAS and ILAS-II legacies. The spectral coverage and resolution of the visible spectrometer are the same as those of ILAS and ILAS-II. However, the wavelength shift due to the temperature change on orbit will be minimized by using the telecentric optical configuration and replacing the grating and lens material. The servo control system of the sun tracking gimbals is also modified. The fast sampling of the sun sensor, faster servo control, and feed forward control will improve the gimbals tracking speed and stability. Other components are newly designed and their laboratory models and engineering models were manufactured and have been tested. This chapter presents the laboratory test results and current status.

### (1) FTS sampling system

**Modulation efficiency.** The modulation efficiency is the key performance of the FTS. The divided beams must be carefully aligned and combined to get high modulation efficiency, which can be measured by comparing the minimum and maximum output signals of the chopped input light source. The tested efficiencies of the laboratory model are 66% at  $975\text{ cm}^{-1}$  and 56% at  $2905\text{ cm}^{-1}$ .

**16-bit analogue to digital conversion.** As the FTS has a wide spectral range and relatively high spectral resolution, high-bit ADC is required. To achieve a quick scan, in other words, high vertical resolution, A/D conversion of about 100,000 samples per second is needed. The A/D converting circuit board with a buffer amplifier and flight ADC chip was manufactured.

Figure 7-12 shows the acquired interferogram at the speed of 80K samples per second together with the data with the commercial high-speed 16-bit ADC. In addition, the bandwidth of the amplifier and ADC was also measured, and found to be larger than 300 KHz with no significant phase delay in the sampling frequency.

**Wavelength calibration with higher spectral resolution FTS.** The instrument function will represent the spectral response of the instrument. It can be measured with a finer spectral interval than the FTS using the monochromatic light source. The tunable diode laser is the ideal monochromatic source with enough power and spectral purity. The input wavelength of the tunable diode laser can be calibrated with the DA8 FTS, which has spectral resolution of  $0.013\text{ cm}^{-1}$  (unapodized). ILSF measurement configuration with a tunable diode laser (TDL) is shown in Figure 7-13. Figure 7-14 shows the measured instrument function by tuning the input current of the laser.

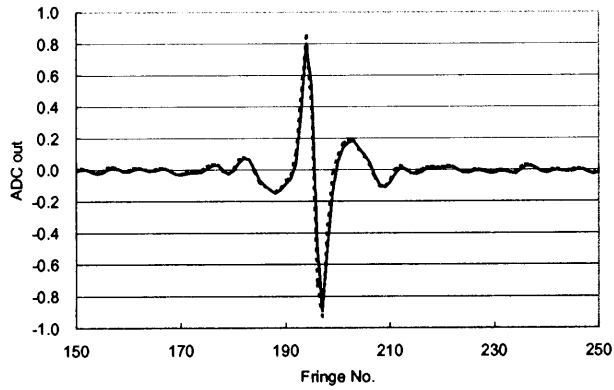


Figure 7-12. Interferogram acquired with the laboratory model FTS, PV-MCT, and 16-bit ADC (solid line) compared with the data with the commercial ADC.

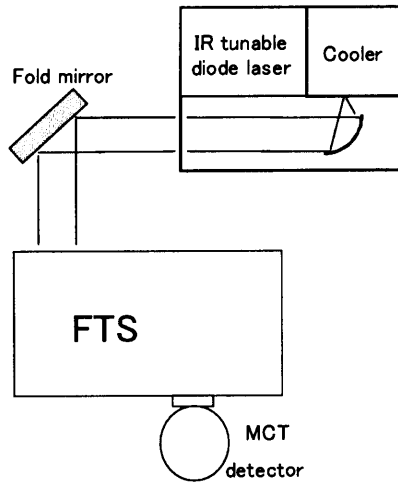


Figure 7-13. ILSF measurement configuration with the TDL.

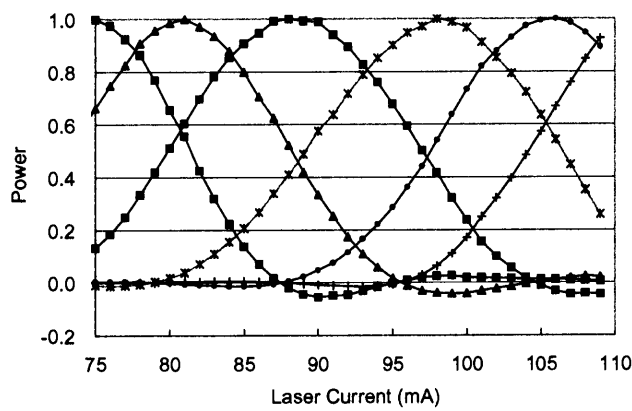


Figure 7-14. Instrument line shape measured with DA8 high resolution FTS and tunable diode laser.

## (2) PV-MCT detector and amplifier

The PV-MCT detector has the following advantages for the FTS application: (1) excellent linearity, (2) low  $1/f$  noise, (3) low heat-dissipation, (4) low offset level, and (5) excellent impedance matching with a preamplifier. The manufacturing of the long wave cut-off PV-MCT uses state-of-the-art technology. Recent advancements in LPE p-on-n MCT backside-illuminated detector technology have extended the cut-off wavelength to 16-17  $\mu\text{m}$ . Figure 7-15 shows the measured cut-off wavelength of the PV-MCT of the laboratory model, which is mounted on a liquid nitrogen dewar. As the output impedance of the detector diode is low, the reverse bias level on the diode and the amplifier must be carefully designed. The detector is connected to the amplifier, which is attached to the dewar directly. The chip of the flight detectors and spare flight detectors has been also selected and diced. These detectors have the cut-off wavelength of 8.3  $\mu\text{m}$  for band 1 and 14.8  $\mu\text{m}$  for band 2.

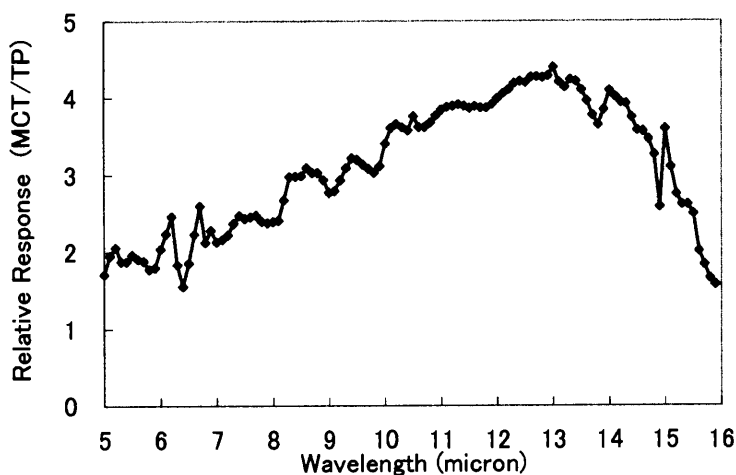


Figure 7-15. PV-MCT laboratory model spectral response compared with a thermo pile detector at the temperature of 79.3 K.

## (3) Pulse tube cooler

The PV MCT detector is cooled to 70 K with the pulse tube cooler on orbit. As the piston motion of the compressor is well balanced up to 16<sup>th</sup> harmonics, the vibration level of the pulse tube cooler is very low. The reduced vibration will minimize the microphonic noise of the IR detectors and disturbance of the FTS during its scan. The piston frequency can be tuned by commands to optimize the cooling capability and avoid the resonant frequency of the instrument. The frequency dependency of the power consumption was measured over the tuning range. The test result of the flight cooler showed excellent cooling capability; without the heat load, it can be cooled below 50 K, and with 1 W heat load less than 50 W was consumed to cool below 65 K. As the instrument uses the PV type detector, the heat load is essentially small and the load including the heat sink from the environment is estimated to be less than 1 W.

#### (4) FTS Laboratory model using liquid nitrogen cooled test detectors.

**Laboratory test.** Test detectors were manufactured and tested. Two different cut-off MCTs are mounted on the liquid nitrogen cooled dewar. The location of the two detectors and dewar window are identical with the flight detector. Figure 7-16 shows the data with blackbody input light source Figure 7-17 shows the achieved SNR data.

**Acoustic test.** There are three moving parts in the instrument: the sun tracking gimbals, the FTS actuator, and the mechanical cooler. There also could exist disturbances from the satellite attitude control system. To estimate the vibration effect caused by the moving parts, the acoustic effect with a vibration source between 70 Hz and 5 KHz has been tested and the noise of the interferogram has been monitored. There exists a small noise response at 135 Hz. However, the retrieved spectra have no significant noise or unexpected signal.

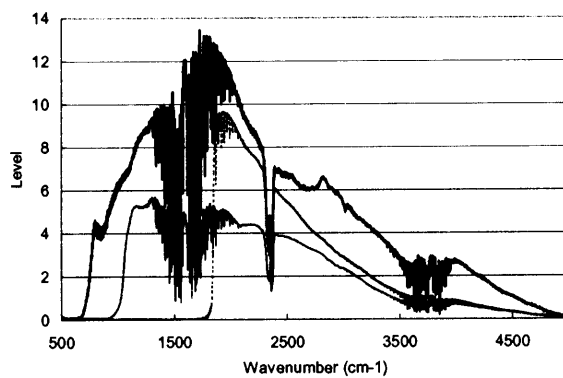


Figure 7-16. Blackbody spectra with three test detectors: SW-PC-MCT (solid line), LW-PC-MCT (bold line), InSb (dotted line).

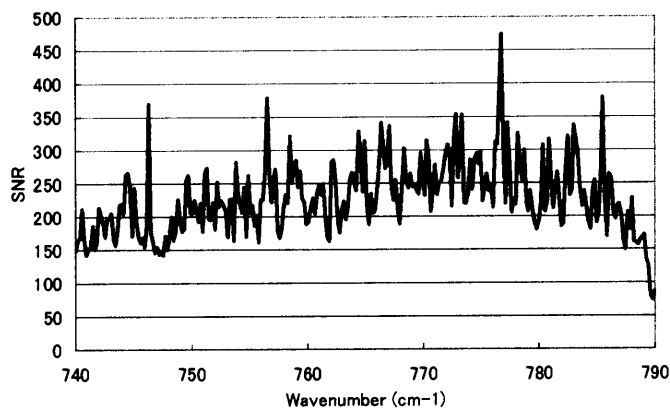


Figure 7-17. Measured SNR with sampling rate 80 KHz using the 800 degrees C blackbody without the telescope.

#### (5) Measured spectra on the ground.

The measured data is the convolution of the instrument function and absorption line spectra. Figure 7-18 shows the measured CH<sub>4</sub> spectra together with the simulated spectra, which is the convolution of the instrument

function and FASCODE 3 output [Clough *et al.*, 1986]. The results show that CH<sub>4</sub> lines are well separated from other constituents and can be retrieved.

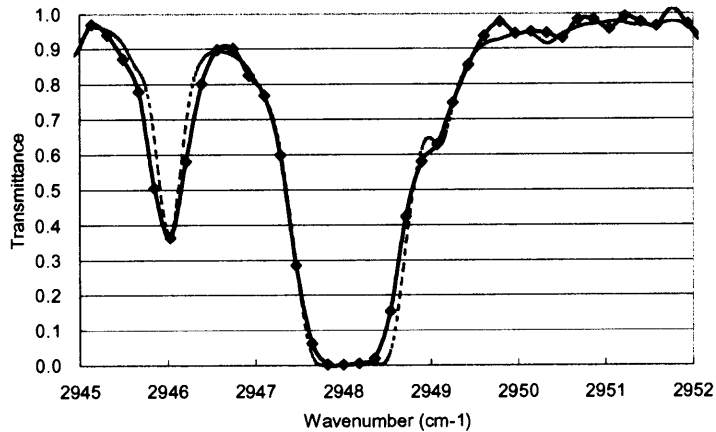


Figure 7-18. Measured CH<sub>4</sub> in Yokohama, Japan, at 10:25 AM, 12, April, 2000 (solid line) together with the simulation (dotted line).

## 7.6. Engineering Model Design Update and Test Results

### (1) Design updates

**Detector and read out.** The MCT detector mounted on liquid N<sub>2</sub> dewar operated at about 80 K was replaced by the 2-pixel PV-MCT detector, which is mounted on the dewar and mechanical cooler assembly and cooled down to 70 K. The dewar is connected to a 3-stage amplifier, which cuts high frequency noise and provides flat-delayed signals over the target spectral range. The trigger signal for AD converting transmitted from FTS controller using a laser fringe is retarded to compensate the delay due to the IR amplifier.

**FTS.** The prism mirror, which doubles the optical path difference, is replaced by the flat mirror of excellent surface quality. This optical configuration improves the alignment capability and the modulated efficiency as described below.

### (2) Engineering model test results.

**Detector and cooler assembly.** 2-pixel PV MCT detector is mounted on the dewar. The focal plane is connected to the cooler head. Figure 7-19 shows the spectral response of the PV MCT detectors compared with the thermo pile detector, which has flat spectral response. These detectors have cut-off wavelength of 8.3  $\mu\text{m}$  for band 1 and 14.8  $\mu\text{m}$  for band 2. Figure 7-20 shows the temperature dependency of the cut-off of the band 2 detector. The focal plane temperature can be tuned by controlling the cooler motor power. The result shows the detector has longer wave cutoff with colder temperature. In addition, colder detector has lower noise. The operating temperature will be tuned at 70K considering both detector performance and cooler power consumption. Detector noise is lower than the FTS mechanical jitter noise At 70K and it is not a dominant noise source.

**Modulation efficiency.** The modulation efficiency is key performance of a FTS. The divided beams

must be carefully aligned and combined to get high modulation efficiency, which can be measured by comparing the minimum and maximum output signals of the chopped input light source. The measured efficiencies of the laboratory model are 71% for band 1 (short wave) and 92% for band 2 (long wave).

**Interferogram.** Figure 7-21 depicts the interferogram acquired with EM FTS and FM detector/cooler assembly using blackbody light source. The results presented excellent symmetry of the interferogram for both band 1 and band 2 and very small phase-delay in amplifier and optics. When comparing between Figure 7-12 and Figure 7-21, the acquired interferogram by the engineering model (flight configuration) has more symmetric than the one acquired with the laboratory model by using the rigid mounting and tuning the optics alignment.

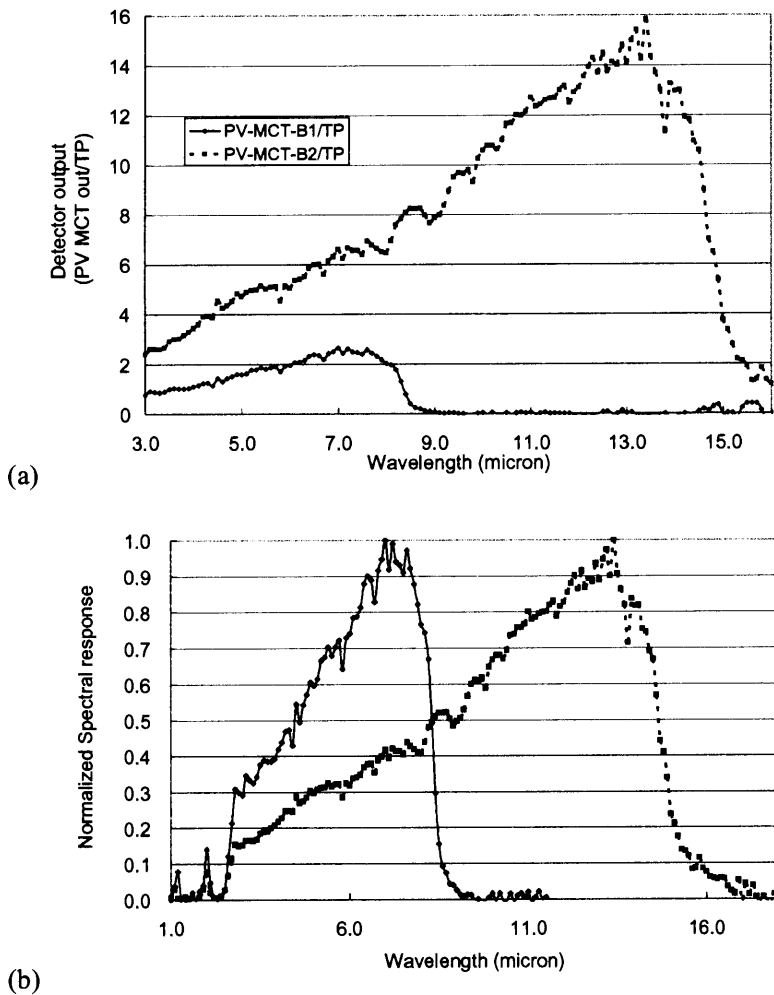


Figure 7-19. (a) Measured spectral response of the band 1 and band 2 detectors mounted on the cooler and detector assembly using a monochromatic light source. The data were divided by the output of thermo pile detector, which is a thermal detector and has no spectral dependency of the response. Note that the band 2 detector (long wave) has 6.8 times higher gain level than band 1 detector. (b) Normalized spectral response.

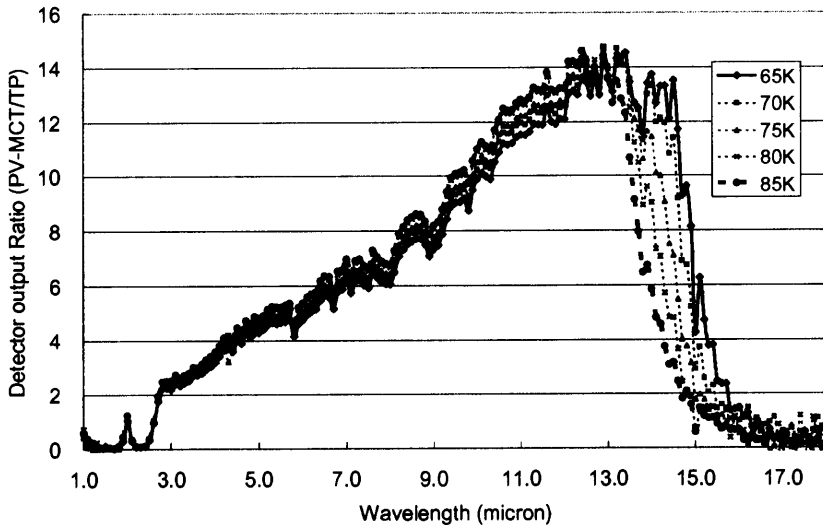


Figure 7-20. Measured temperature dependency of the long wave detector cut-off using a monochromatic light source.

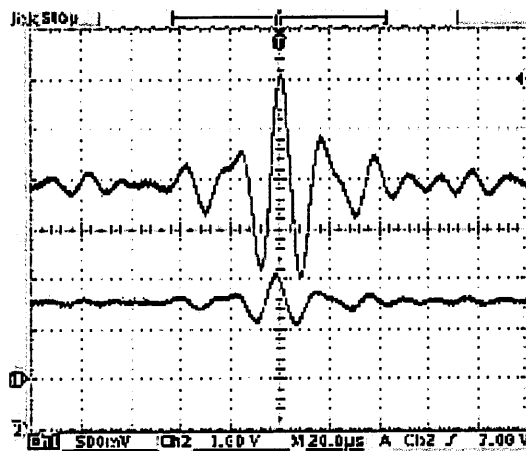


Figure 7-21. Band 1 (lower) and band 2 (upper) interferograms acquired with the engineering model using a 1473 K blackbody light source.

### (3) 5000-pixel CCD for the sun edge sensor

The 5000-pixel Si-CCD and its driver circuit acquire the sun edge data. The monitoring wavelength is 750 nm, which is the atmosphere window region. Thus the sun edge light, which passes through the lower atmosphere, can be detected. The CCD is driven with a 1 MHz clock and the integration time is 50 msec. The analogue signal is converted to the 12-bit digital signal. The one-dimensional array CCD, its electronics, and 12-bit ADC were manufactured and their performances were acquired. The measured cut-off wavelength is 1120 nm.

#### (4) Integration of the space qualified components

Figure 7-22 shows the integration flow and its current status of the components. Most components of the Engineering model have been manufactured, integrated, and tested.

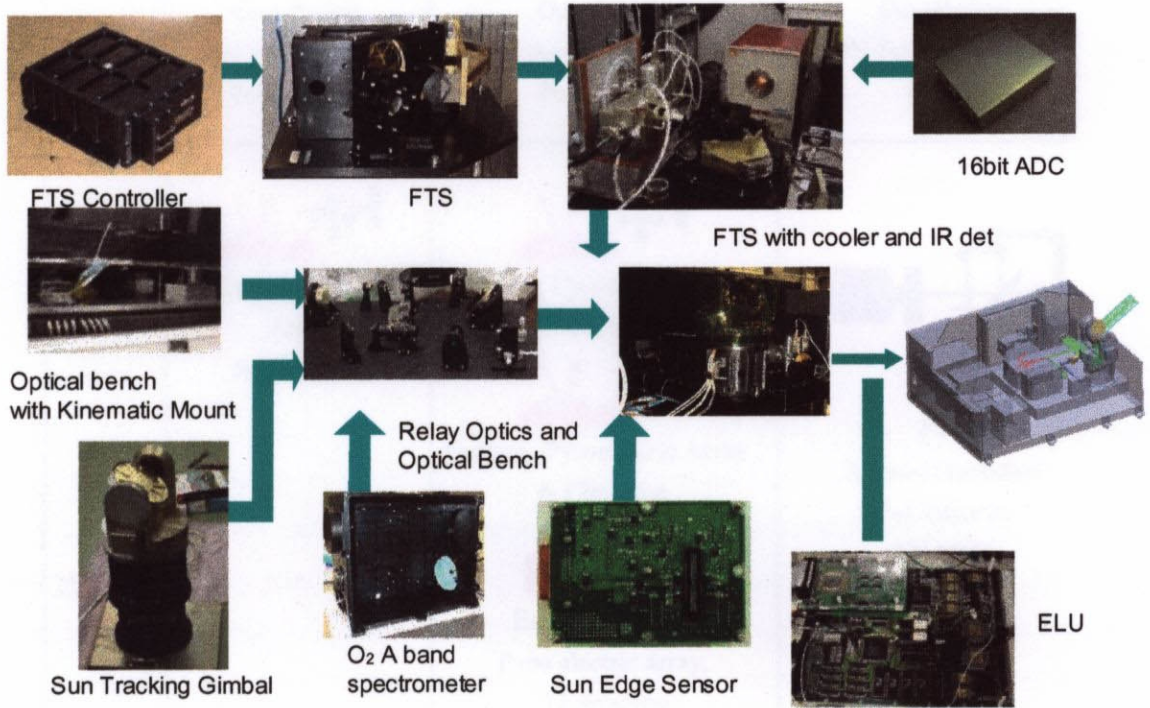


Figure 7-22. The integration flow and its current status of the components.

### 7.7. Conclusion of this Chapter and Expected Scientific Results

The instrument will provide vertical profiles of atmospheric constituents globally with high vertical resolution and moderate spectral resolution. As illustrated in Figure 7-23, it will succeed the ILAS and ILAS-II high latitude measurements. It will also monitor the distribution of greenhouse gases in both of the stratosphere and upper troposphere. It uses a combination of the well-proven FTS and state of the art PV-MCT technology. The key components were manufactured and their performance has been tested. The instrument is expected to be a robust system that will provide long-term monitoring data. The robust design FTS will also provide wide continuous spectra data with moderate resolution. In addition, the high frequency and feed forward gimbals control system will enable accurate and stable tracking from lower altitude. The combination of visible spectrometer and sun edge sensor will improve the height retrieval.

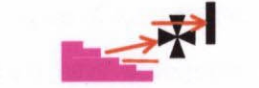
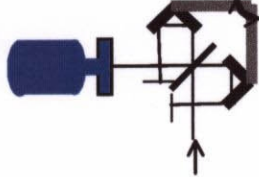
	ADEOS/ILAS	ADEOS-II/ILASII	Solar Occultaion FTS
Method	 <p>Occultation Sun-synchronous, Polar region</p>	 <p>Occultation Sun-synchronous, Polar region</p>	 <p>Occultation NON-Sun-synchronous, Global</p>
IR	 <p>Grating, Pyroelectric Array 6-12micron</p>	 <p>Grating, Pyroelectric Array 3-6micron</p>  <p>Grating, Pyroelectric Array , 6-12micron</p>  <p>Echelle Grating, Pyro electric array, 12.8micron</p>	 <p>FTS 0.2cm-1resolution 3-13micron PV-MCT</p>
Visible			

Figure 7-23. Heritage of ILAS and ILAS-II and advancement.

# Chapter 8 Appendix III. Compact Fourier transform spectrometer for 3 dimensional monitoring of greenhouse gases

-Direct observation method of greenhouse gases in troposphere -

Considering global increase in greenhouse-gases, observation and monitoring of the earth's atmosphere with space-borne instruments are essential. Satellite measurement offers the advantage of global and long-term monitoring. In the short wave infrared (SWIR) region of 1.6-1.9  $\mu\text{m}$ , major greenhouse gases (carbon dioxide ( $\text{CO}_2$ ), water vapor ( $\text{H}_2\text{O}$ ), and methane ( $\text{CH}_4$ )) have absorption spectra of moderate strength without interference by other molecule absorption. In addition, we can use the un-cooled detector for this wavelength region. Two different types of observation geometry will be discussed; one is nadir-looking with sun glint light source for the column amount retrieval and the other is limb-looking with scattered light source for the vertical profile retrieval. A four-ports Fourier transform spectrometer (FTS) for this application is proposed. One input port is for nadir-looking measurements and the other input port is for limb-looking measurements. One output port is used for greenhouse gases measurements and the other port is used for the oxygen ( $\text{O}_2$ ) absorption spectra measurement for the optical path length calibration. The instrumentation of the FTS, retrieval algorithm, and expected performance are discussed, and ground test results are also presented.<sup>1</sup>

---

<sup>1</sup> This chapter has been published in "Measurement of greenhouse gases from space with a SWIR FTS," *SPIE* **4485**, 69-80, (2002) and was co-authored by Y. Sasano, H. Nakajima and M. Suzuki. It was updated and revised.

## 8.1. Introduction

For optical remote sensing applications, there are several methods of observing the atmospheric constituents from the UV to far infrared region. To monitor the greenhouse gases frequently and accurately, a fast observation method must be investigated. The UV spectra with the scattered light source are mainly used for O<sub>3</sub>, NO<sub>2</sub>, and SO<sub>2</sub>. The well-matured Si detector technology can be applied for the UV spectrometer. Total column amount of O<sub>3</sub> can be measured with UV longer than 300 nm. Backscattered UV, which is shorter than 300 nm and mainly scattered in the stratosphere, is used for vertical profile retrieval. These spectra are very weak and the retrieved vertical resolution is limited. In addition, there are no absorption spectra of greenhouse gases in UV except for O<sub>3</sub>. In the thermal and far infrared regions, there are many lines of greenhouse gases, which detectors have enough sensitivity to detect. However, the detectors of these wavelength regions must be cooled below 100 K with a mechanical cooler or a large radiative cooler. Furthermore, for the profile retrieval, the temperature profile must be measured or modeled at the same time. There also exist absorption lines in the short wave infrared region. In this chapter, the advantages of observation frequency, instrumentation, data retrieval, and data accuracy of the SWIR region will be discussed.

The observation method and geometry also must be investigated for SWIR application. The solar occultation method provides comprehensive observation measurements for vertical profile retrieval. However, there are only two solar occultation events per orbit, so it is difficult to monitor the global distribution in a short period. Nadir-looking scattered light measurement is the fast method used for global observation. The measured radiance includes the reflected light on the ground in the visible and SWIR regions if the surface is diffusive (Lambertian), and so the sensitivity, in other words, retrieval accuracy of measuring the atmosphere will be degraded. Thus this method is limited to the UV region, where most of the scattered light is the path radiance and the earth's surface shows little spectral dependency. There are two methods of using the SWIR region to measure greenhouse gases; one is to measure Rayleigh scattering by limb-looking to maximize the sensitivity, and the other is to measure the sun glint by nadir-looking for the column amount retrieval [Aoki *et al.*, 2001]. Limb-looking measurement has a long optical path and sun glint measurement has a high spectral radiance. As the resources (size, weight, power, and data-rate) are limited for space-borne instruments, the FTS is appropriate for this application. The advantages of the FTS and its instrumentation will be discussed.

### (1) Line parameters and spectral resolution

This section describes the advantages of using SWIR for monitoring greenhouse gases and presents the results of a sensitivity study.

**Narrow spectral region.** Between 1.6 and 1.9  $\mu\text{m}$ , absorption spectra of three major greenhouse gases exist. As the spectral region is limited, the aliasing problem of the FTS can be removed. In addition, under-sampling can be applied to reduce the data rate. Furthermore, the dynamic range that is needed for the multiplexed spectra of the FTS can be optimized.

**Strength.** For measurement of the troposphere where air mass is large, relatively weak lines are adequate.

Moderate strength absorption will give sufficient sensitivity and a high signal-to-noise ratio (SNR). CH<sub>4</sub> is measured at 6003 cm<sup>-1</sup>, and CO<sub>2</sub> at around 6215 and 6359 cm<sup>-1</sup>. In addition, there exist continuous H<sub>2</sub>O absorption lines between 5400 and 5920 cm<sup>-1</sup>. Figure 8-1 (a) shows line intensity of the target constituents between 5500 and 6500 cm<sup>-1</sup> [Rothman et al., 1998]. Figure 8-1 (b) also depicts the temperature dependency of CO<sub>2</sub> line intensity. The data shows less temperature dependency than other spectral region and these characteristics can minimize the error caused by uncertainty of temperature vertical profile.

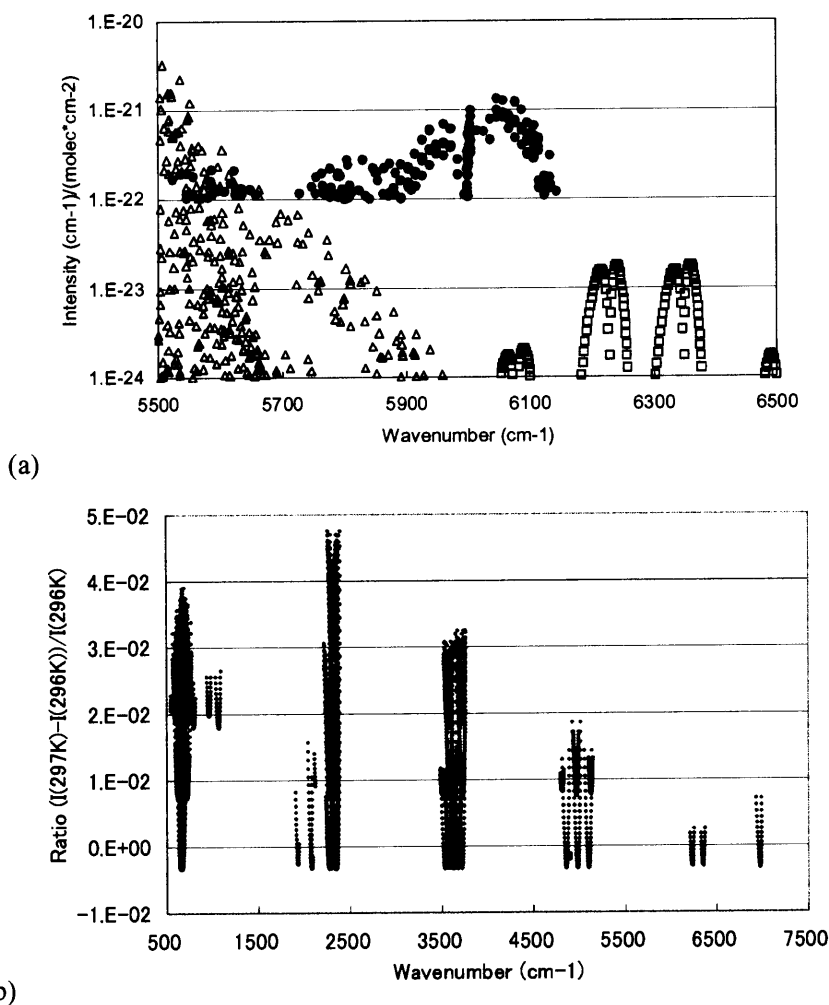


Figure 8-1. (a) Line intensity of CH<sub>4</sub> (circle), CO<sub>2</sub> (square), and H<sub>2</sub>O (triangle) and (b) Temperature dependency of CO<sub>2</sub> line intensity at 296K.

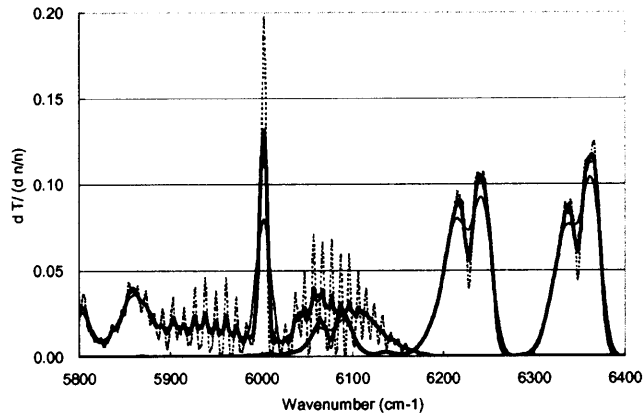


Figure 8-2.  $\text{CH}_4$  and  $\text{CO}_2$  sensitivity of spectral resolution: 4 (solid line), 8 (bold line), and 16 (dotted line)  $\text{cm}^{-1}$  cases.

**Interference (isolation).** In this region,  $\text{CH}_4$ ,  $\text{CO}_2$ , and  $\text{H}_2\text{O}$  absorption lines do not interfere with each other. Therefore these three gases can be retrieved independently.

**Required spectral resolution.**  $\text{CH}_4$ ,  $\text{CO}_2$ , and  $\text{H}_2\text{O}$  have several absorption lines, which are adjacent to each other. To extract each line independently, very high spectral resolution is required. However, by averaging the several lines, moderate resolution is sufficiently sensitive to detect the gases. The sensitivity can be defined as  $dT/(dn/n)$ , where  $T$  is the transmittance between outer space and the ground. Figure 8-2 shows the  $\text{CH}_4$  and  $\text{CO}_2$  sensitivity of the spectral resolution for 4, 8, and 16  $\text{cm}^{-1}$  cases assuming the air mass factor of 3 and using MODTRAN3 [Berk *et al.*, 1989]. The results show that there is no significant difference between 4 and 8  $\text{cm}^{-1}$  resolution and 8  $\text{cm}^{-1}$  is enough to detect the vertical profile of the greenhouse gases.

## 8.2. Observation Geometry

This section presents the SWIR observation method using an FTS in space.

### (1) Limb-looking measurement

Limb-looking measurements will provide the vertical distribution and produce a large optical path, in other words, large optical thickness can be acquired. It is assumed that multiple scattering of SWIR is negligibly small because of the small Rayleigh scattering coefficient. Figure 8-3 shows the observation geometry and vertical profile measurement concept using a one-dimensional array detector. By observing limb-scattered light and scanning the tangent points electrically with one dimensional array detector, the vertical profile can be retrieved from orbits. As the field of view is wide, the wavelength measured with off-axis pixels must be calibrated. As scattered-light measurements use direct absorption, the high vertical resolution with high accuracy can be expected. Compared with the solar occultation method, longer observation time and thus higher SNR as well as frequent measurements can be achieved.

## (2) Nadir-looking measurement

To monitor greenhouse gases, it is essential to measure the troposphere where the greenhouse effect occurs. In general, it is more difficult to measure the troposphere from space than the stratosphere. Nadir-looking measurement is the only feasible way to measure the flux that passes through the lower troposphere. Figure 8-4 shows the geometry of nadir-looking measurements. The measured radiance consists of the path radiance and the surface reflection. When the surface is Lambertian, it is hard to extract the surface reflection part from the measured spectra. On the other hand, if the surface is specular, the surface reflection (sun glint) is dominant and the flux that passes through the troposphere can be measured. From space, sun glint will exist on the sea surface where the solar flux is reflected back to the satellite. Thus, a sun-glint point always exists and the instrument can track the point continuously. As the sea surface is not flat due to wind, the reflected light is dispersed and the reflected flux has a cone-like structure (sun-glint cone). To increase the measurement opportunities, sun glint on large lake surfaces could also be used.

## (3) Field of view requirement

Assuming the altitude of the satellite orbit to be 600 km, this instrument will view the vertical profile between ground and the tangent height of 100 km simultaneously from about 3000 km away, thus a 30-mrad field of view will be required.

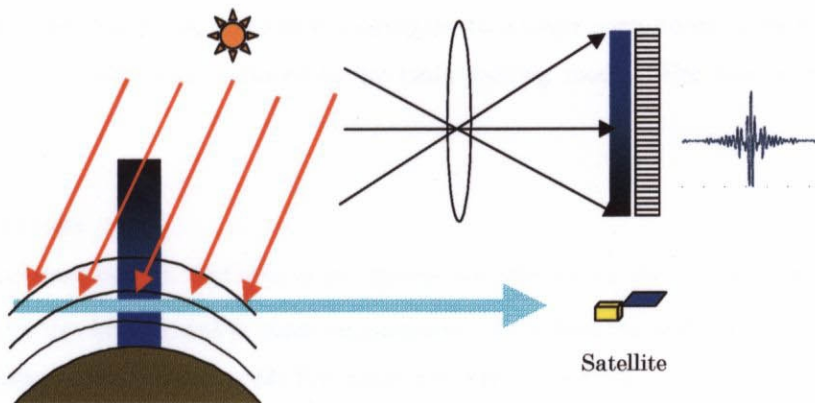


Figure 8-3. Limb-looking observation geometry.

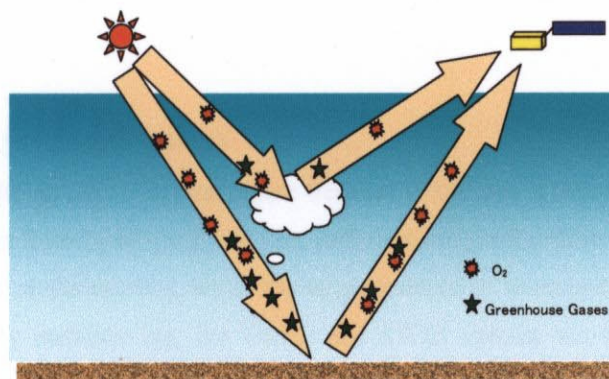


Figure 8-4. Nadir-looking observation geometry.

### 8.3. Instrumentation

In this section, the conceptual design of the space-borne FTS, the related optics and operation are discussed.

#### (1) Configuration

Table 8-1 shows the instrument specifications. Figure 8-5, Figure 8-6, and Figure 8-7 show the FTS optics configuration, instrument concept, and block diagram, respectively. Assuming a sun-synchronous orbit, in the limb-looking mode, the FTS will point in the direction away from the sun to view the back scattering, while in the nadir-looking mode, the instrument has to view the sun-glinton point in the direction of the sun. Therefore, the instrument has to be mounted on the satellite with two different fields of view.

#### (2) Fore-optics

This instrument has two fields of view: nadir and limb. For nadir-looking measurements, the instrument has to track the sun-glinton point. The two-axis gimbals will flip its mirror toward the direction where the sun glinton is expected to occur. As the satellite altitude is very stable, the limb-looking mode does not need a tracker. However, as the scattered light is weak, a telescope has to be used to collect more light than in the nadir-looking mode. Using the 4-ports system described below, two different scene fluxes can share the same detector. As shown in Figure 8-5 and Figure 8-6, in the limb-looking mode, a larger aperture telescope is installed. A shutter is inserted at the focal point and is closed in the nadir-looking mode. The flux is collimated again and introduced to the FTS.

#### (3) SWIR advantage

**Detectors without cooler.** InGaAs is an appropriate detector for the region shorter than  $2\ \mu\text{m}$ . This photon type detector can be operated at room temperature. To reduce the dark current, the detector is cooled using a thermo-electric cooler, which needs few electric power and weight.

**Optics material.** For the SWIR ( $1.6$  and  $1.9\ \mu\text{m}$ ) and visible ( $760\ \text{nm}$ ) wavelength regions, durable materials can be used for application in space. For the beam splitter and the compensator substrates, nonhygroscopic BK7 glass will be used. Other optics elements are reflective optics, which have no achromatic aberration.

#### (4) FTS advantages and proposed system

A FTS is selected as the space-borne instrument because it has two advantages: high throughput and multiplexing [Bell, 1972]. For limb-looking application, sufficient integration time is secured due to the stable orbit and same tangent height of the satellite, while the large aperture of telescope and wide horizontal view ensure a high throughput. By multiplexing, the visible and SWIR spectra can be covered with only two detectors. As the spectral resolution is moderate ( $8\ \text{cm}^{-1}$ ) and obliquity limit is large enough to cover the atmosphere profile from the ground to outer space, imaging FTS technology with an array detector can be

applied. In addition, as the moving distance is limited, both sides of the optical path difference can be scanned. A conventional commercial FTS instrument with four ports can be modified for space application. One input port is for nadir-looking measurements and the other input port is for limb-looking measurements. One output port is used for SWIR measurements and the other output port is used for the O<sub>2</sub> absorption spectra measurement for the optical path length calibration. A 1.55 μm laser diode qualified for space use will provide the fringe, which is the sampling trigger for analog to digital conversion (ADC) of the detector signal. The scanning direction is also detected from the dephase laser fringes. To stabilize the wavelength, temperature of the laser is controlled. The Nyquist frequency will become 3,326 cm<sup>-1</sup>, therefore 1.6 and 1.9 μm spectra are folded. The second-order spectra will be used for this spectral band. As the bandwidth is narrow enough, the under-sampling of the interval of 2 or 3 will be possible. The O<sub>2</sub> spectra at 760 nm can be detected as the order of 3 spectra. InGaAs and Si detectors, which are mature technologies, can be used.

Table 8-1. Instrument parameters.

Target	CH <sub>4</sub> , CO <sub>2</sub> , H <sub>2</sub> O, and O <sub>2</sub>
Wavelength region	760 nm (or 1.25 μm) 1.6-1.9 μm (5200-6400 cm <sup>-1</sup> )
Spectral resolution	8 cm <sup>-1</sup>
IFOV	0.3 mrad for limb-looking (1 km in tangent height)
Fore-optics	10 mm pointing mirror (nadir) 100 mm telescope (F=5)(limb)
Fourier transform spectrometer	Double corner cube BK7 beam splitter
Sampling laser	1.55 μm diode laser
SWIR detector and its specific detectivity	InGaAs 273K (Thermo-electric cooled) 1D array (limb-looking) <i>D</i> * greater than 4×10 <sup>12</sup> cmHz <sup>1/2</sup> / W

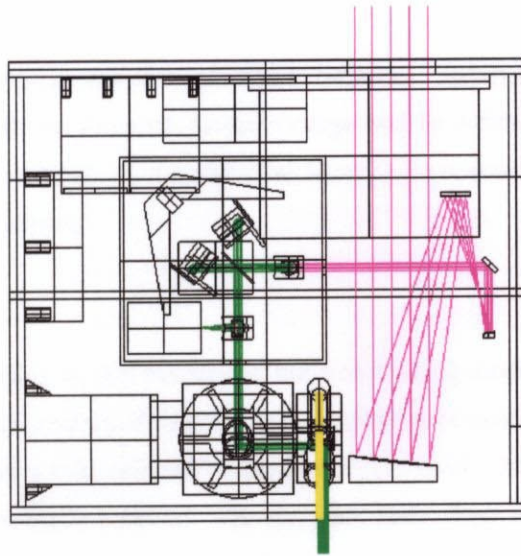


Figure 8-5. Concept of space-borne FTS.

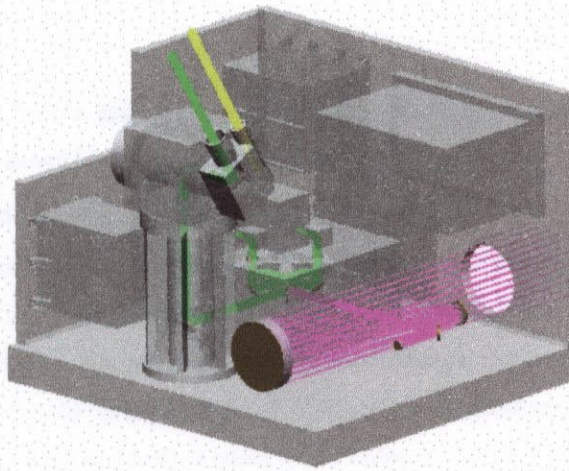


Figure 8-6. Space-borne instrument.

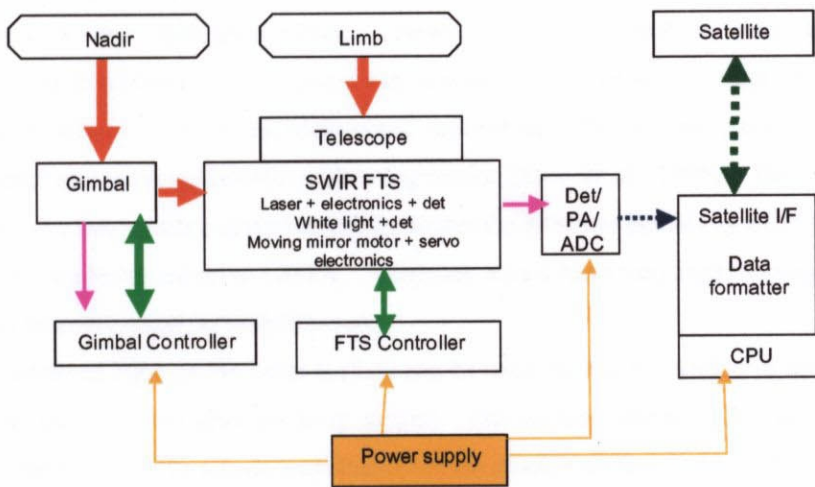


Figure 8-7. Instrument block diagram.

## (5) Signal processing

The spectral range of this measurement is from 5200 to 6400  $\text{cm}^{-1}$  and the spectral resolution is 8  $\text{cm}^{-1}$ . Assuming the required SNR is 300, the required dynamic range will be 3700, therefore, at least 12 bits is required for ADC. Considering variation in the sun-glint level and uncertainties in orbit, a 16-bit ADC converter will be used for this application.

## (6) Operation

There are two operational modes for this instrument: the limb-looking mode and the nadir-looking mode. The input level from the low scattered radiance to the high sun-glinton radiance needs a wide dynamic range. The gain of the amplifier of the detectors will be selected based on the input level. For nadir measurement, the sun glint changes quickly, so fast scanning is required. On the other hand, limb-looking measurements, whose radiance level is very weak but stable, need a large integration time. The gain level and the scanning speed will be optimized by commands issued from the ground.

## 8.4. Calibration

For the purpose of tuning before launch and long-term monitoring after launch, both radiometric and spectral calibrations must be considered both on the ground and in orbit.

### (1) Radiometric calibration

For nadir-looking measurements, the radiance of the measured light source depends on the sea surface condition. The typical levels of the surface albedo of sun glint are 900% and the spectral radiance at 6000  $\text{cm}^{-1}$  is equal to that of 900 K blackbody. For vertical profile measurements, the input level depends on tangent height. When the instrument views the tangent height of 10 km and no absorption by atmospheric constituents is assumed, the equivalent albedo is 30%, which is equal to the radiance of 675 K blackbody.

**On the ground.** As the dynamic range of the scene flux is large, the radiometric response must be calibrated by tuning the blackbody temperature. The ideal standard is a cavity blackbody with an aperture that covers the diameter of the instrument optics. However, it is difficult to manufacture a large and high-temperature cavity blackbody and to control the temperature uniformly. A high-temperature blackbody and collimator system will be used for the radiometric calibration. This system consists of a graphite cavity blackbody light source and a silicon carbide collimating mirror [Kuze *et al.*, 1996]. The mirror temperature is controlled to be the same temperature as the blackbody so that the effective emissivity will be close to 1.00. The mirror and blackbody can be heated up to 1000 K. Tungsten, which has a very high melting point, is selected as the coating material to avoid metal recrystallization.

**On orbit.** Scattered light on the lunar surface can be used for the calibration in orbit. The instrument will track the moon using its sun-glinton tracking gimbal. The surface albedo is 7% and the surface can be assumed to be Lambertian. As the albedo distribution on the moon's surface is not uniform, the reflected light must be averaged by seeing the whole surface.

## (2) Wavelength calibration

The instrument function represents the spectral response of the FTS. As the spectral resolution of the instrument is wider than the absorption line width of the atmospheric constituents and there are several lines within one spectral channel, the spectral response of the instrument must be carefully calibrated. Using the array detector, the spectral position acquired by the off-axis pixels will be shifted from the center pixel, because the optical path is slightly different from that of the reference laser. The instrument function of each pixel must be characterized. The ideal instrument function of the FTS is the sinc function. However, for this application, the field of view is wide and the instrument function will be distorted due to the off-axis effect. Therefore the instrument line shape function will be measured with a tunable monochromatic light source (tunable diode laser). The wavelength of the monochromatic light source will be calibrated with a higher resolution FTS [Kuze *et al.*, 1998].

## 8.5. Retrieval Algorithm

This section presents the algorithm used for retrieving the column amount and the vertical profile.

### (1) Retrieval flow

Figure 8-8 shows the air mass factor and greenhouse gases retrieval flow using the visible and SWIR spectra acquired with the FTS in orbit. The mathematical retrieval model includes the target gas vertical profile model and other physical parameters. The Rayleigh scattering coefficient is modeled as shown in Figure 8-9 [Bates, 1984, Bucholtz, 1995, and Nicolet, 1984].

### (2) Optical path length and cloud detection

The distribution of molecular oxygen can be assumed to be a known parameter. Using the measured optical thickness from O<sub>2</sub> absorption in the visible region or in SWIR, the key parameters such as the optical path length, in other words, air mass factor and cloud heights can be retrieved [Kuze *et al.*, 1994]. Radiance of both greenhouse gases and O<sub>2</sub> measurements can be expressed as follows.

$$I_{\lambda} = \int F_{\lambda} f_{\lambda} \exp[-s\alpha_{i\lambda}n_i] d\lambda, \quad (8-1)$$

where  $F_{\lambda}$  is the solar irradiance,  $f_{\lambda}$  is the instrument function of the FTS,  $\lambda$  is the wavelength, the suffix  $i=1$  is for greenhouse gases measurements and  $i=2$  for O<sub>2</sub> measurements,  $\alpha_{\lambda}$  is the gas absorption coefficient, and  $n_i$  is column amount. By using O<sub>2</sub> measurements, the air mass factor  $s$  is retrieved.

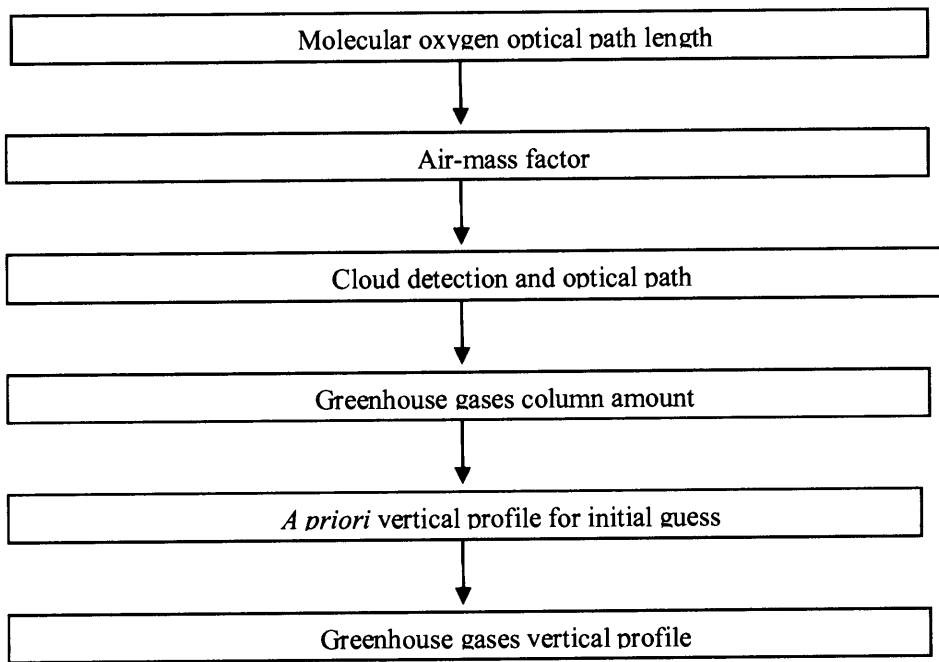


Figure 8-8. Retrieval flow of total column amount and vertical profile retrieval.

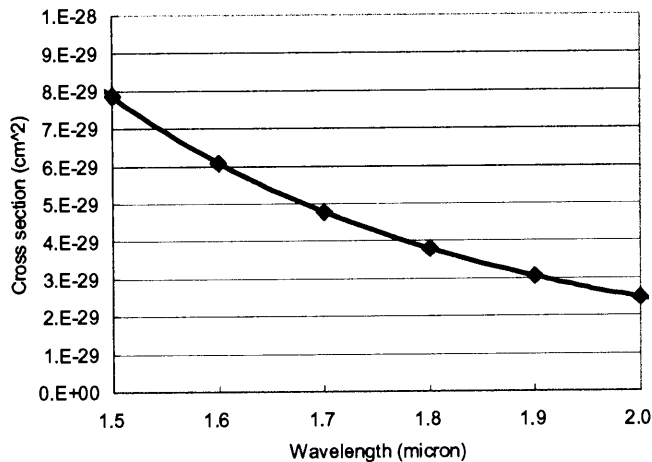


Figure 8-9. Spectral characteristics of Rayleigh scattering cross section [Bucholtz, 1995].

### (3) Vertical profile retrieval

The mathematical retrieval study utilizes the single scattering radiative transfer model. The measured scattered spectra from the orbit are the sum of the light on the path from beyond and from the tangent point. As the Rayleigh scattering coefficient is small in SWIR, these input spectra  $I_{\lambda}$  can be described as following single scattering formula.

$$\text{From the tangent point: } I_{a\lambda} = \frac{1}{4\pi} F_{\lambda} \beta_{\lambda} P(\cos \theta_0) \int_{p_0}^1 s_2 \exp[-(s_1 + s_2)(\alpha n(p) + \beta p)] dp, \quad (8-2)$$

$$\text{Beyond the tangent point: } I_{b\lambda} = \frac{1}{4\pi} F_{\lambda} \beta_{\lambda} P(\cos \theta_0) \int_{p_0}^1 s_2 \exp[-(s_1 + s_2)(\alpha n(p) + \beta(2p_0 - p))] dp, \quad (8-3)$$

where  $p_0$  is normalized pressure,  $p_0$  is the pressure of the tangent point,  $\theta_s$  is the solar zenith angle,  $\beta_\lambda$  is the Rayleigh scattering coefficient,  $P(\cos \theta_0)$  is the Rayleigh phase function, and  $n_p$  is the column methane amount above  $p$ . The optical path (air mass) factors  $s_1$  and  $s_2$  are  $\sec(\theta_v)$ , and  $\sec(\theta_v) + \sec(\theta_s)$  respectively, where  $\theta_v$  is the looking angle.

**Inversion.** The vertical profile is obtained by iteration, comparing measured values with values calculated using the above forward model. The profile retrieval is, in general, a nonlinear problem. Near the solution, however, it is possible to use a linearized form for the retrieval iteration equation:

$$y = y_n + K(x - x_n), \quad (8-4)$$

where  $y$  is the vector of measured values for  $I_\lambda$ ,  $y_n$  is the vector of values for  $I_\lambda$  calculated from  $x_n$ ,  $K_n$  is the weighting function matrix (Figure 8-10),  $x$  is the vector of  $x(p)$  values for the solution profile, and  $x_n$  is the vector of  $x(p)$  values for the profile at iteration  $n$ . The optimum statistical method using *a priori* covariance  $S_x$  and instrumental noise covariance  $S_e$  is used to solve for the profile, giving both height resolution and full precision [Rodgers, 1976 and Rodgers, 1990]:

$$x_{n+1} = x_0 + S_x K_n^T [K_n S_x K_n^T + S_e]^{-1} [y - y_n - K_n (x_0 - x_n)], \quad (8-5)$$

For SWIR retrievals we can use an almost arbitrarily high number of pressure levels, which represent height resolution, because this instrument has many scenes with electrical scanning of the tangent points. However, there exist a number of layers beyond which no effective increase in information, except for precision, is obtained [Twomey, 1977]. The contribution function represents the height resolution and it is calculated to be approximately 2 km. As scattered-light measurements use direct absorption, the high vertical resolution with high accuracy is expected.

**Averaging kernels and height resolution.** The retrieved profile  $x_n$  is the combination of the *a priori* profile  $x_0$  and true profile  $x_t$ , and is described by the following:

$$x_n = x_0 + D_y K_n^T (x_t - x_0) = A x_t + (U - A) x_0, \quad (8-6)$$

where  $D_y$  is the function defined as  $D_y = \frac{\partial X}{\partial y}$ ,  $A$  is the averaging kernel matrix, and  $U$  is the unit matrix. The

contribution function can be defined as  $C = \frac{\partial y}{\partial \log p}$ . Figure 8-11 shows the contribution function of the

limb-looking measurement. The above equation shows that when the averaging kernel is nearly a unit matrix, the *a priori* constraint is weak and a nearly true profile is obtained. It also indicates that the averaging kernel is a transfer function matrix for profiles, and that eigenvector analysis is helpful for understanding height resolution (Figure 8-12).

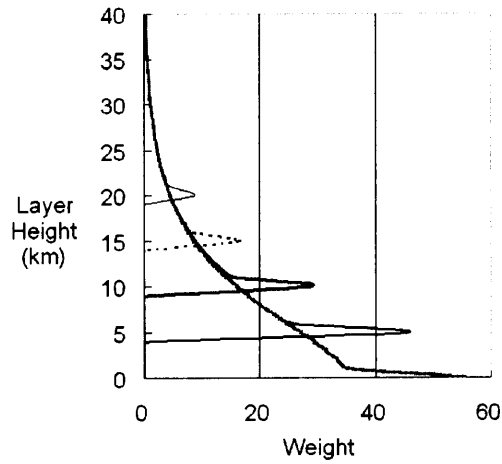


Figure 8-10. The weighting function of limb-looking measurement (tangent height of 0 km, 5 km, 10 km, 15 km, and 20 km).

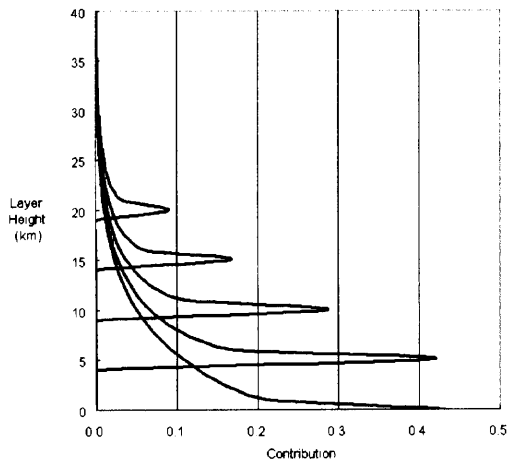


Figure 8-11. The contribution function of limb-looking measurement (tangent height of 0 km, 5 km, 10 km, 15 km, and 20 km).

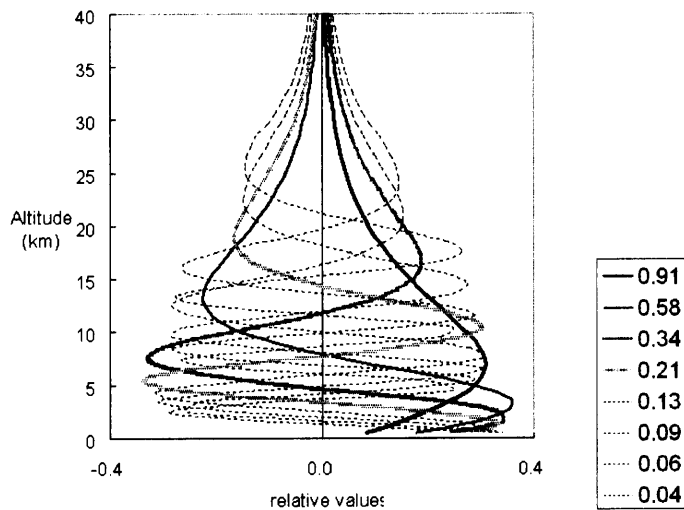


Figure 8-12. The numerically simulated first 8 eigen vectors and eigen values of the averaging kernel matrix.

#### (4) Cloud and aerosol contamination

The above model simulation assumes the clear sky condition. Most of the scenes are contaminated by clouds and aerosols for tropospheric measurements of both nadir and limb views. These contaminations must be detected and corrected with O<sub>2</sub> A band absorption data. The details are discussed in section 8.6.

### 8.5.2. Ground-based Test with the Laboratory Model

The scattered light of the atmosphere, sun-glint light on the sea surface, and the diffusive reflected light on lands were measured with the laboratory model to demonstrate the feasibility of the measurements from the orbit. The specifications of the laboratory instrument are the same as those of the flight instrument in Table 8-1 except for the detector.

#### (1) Ground-based test for demonstration of sun glint measurements

BOMEM MB160 FTS is used as the laboratory model on the ground. It collects scattered and reflected lights with an uncooled InGaAs detector. Skylight and the moon are used as the light sources. To increase SNR, the gain level is maximized and acquired interferograms are averaged. The spectra scattered by the earth's atmosphere on the ground are shown in Figure 8-13. Figure 8-14 shows the spectra for moon light, which is scattered on the moon's surface. The radiance variation is due to the non-uniformity of the moon's surface. In both cases, the moderate absorption spectra of CO<sub>2</sub>, H<sub>2</sub>O, and CH<sub>4</sub> are clearly detected. From the orbit, limb-looking scattered radiance has the level between the one measured on the ground and that of the moon. The above results demonstrate the feasibility of limb-scattered light measurements for globally monitoring the vertical profile of greenhouse gases with 8 cm<sup>-1</sup> spectral resolution from space.

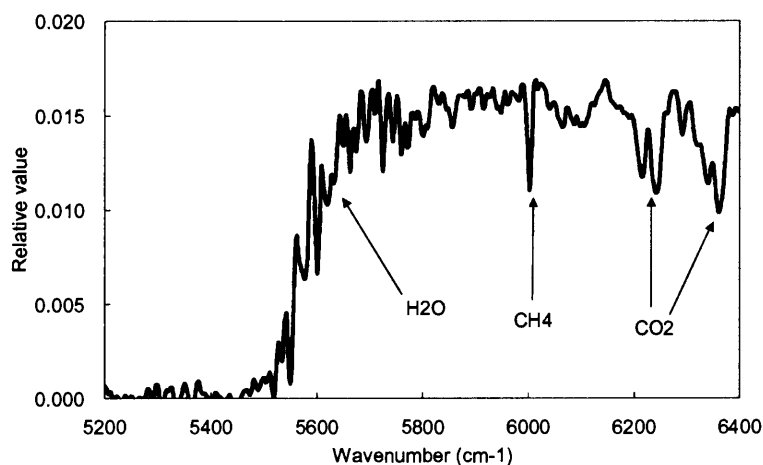


Figure 8-13. Limb-looking scattered light spectra at University of Tokyo on 22, February 1997 16:53 JST. Spectral resolution is 8 cm<sup>-1</sup> and the viewing zenith angle is 70 degrees looking to the east.

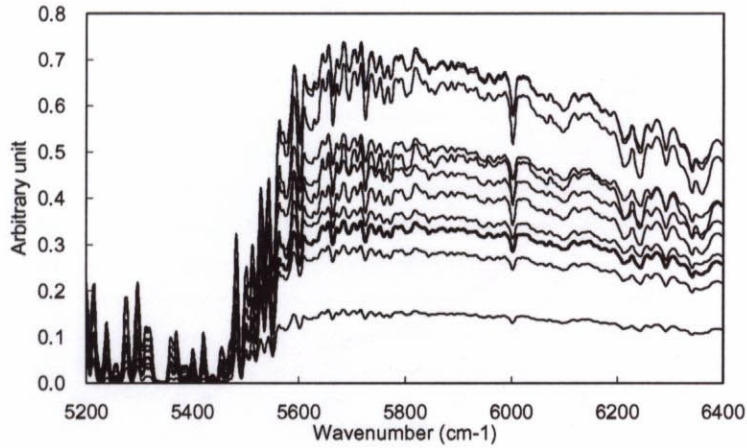


Figure 8-14. Moon light-source observation data of one hour interval at University of Tokyo on 22 and 23, February, 1997.

## (2) Ground-based test for demonstration of sun glint measurements

The sun glint is measured using the same instrument as the scattered light, with the input optics looking at the sun-glint point. Figure 8-15 shows the sun glint measurement geometry on the ground, which has large incident and reflection angles. Figure 8-16 depicts the simulated reflectivity of the earth surface in the case of refraction index of 1.33. This figure indicates that the surface albedo is high for large incident angle on the ground at the sunset or sunrise. In contrast, it is about 0.02 for small incident angle of the satellite observation geometry. Therefore, SNR on orbit have to be carefully estimated because the reflected light is weaker than on the ground.

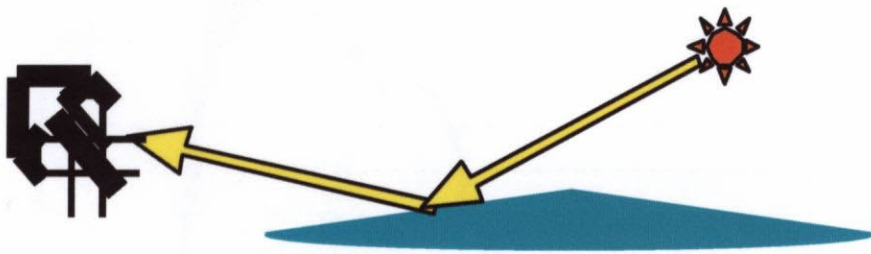


Figure 8-15. Sun-glint measurement geometry of the ground test.

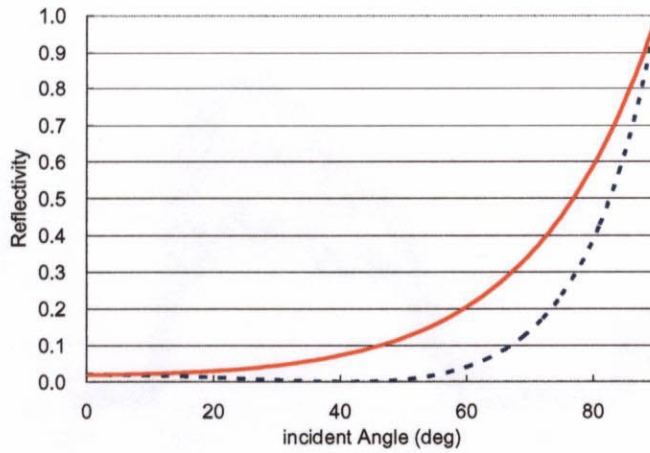
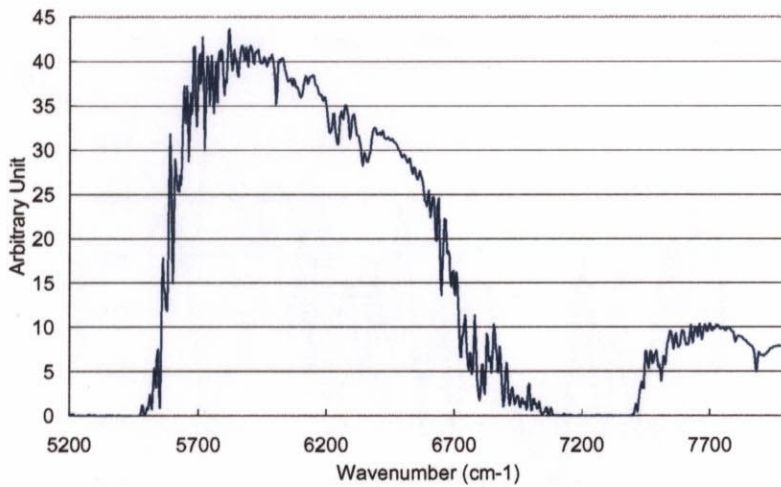
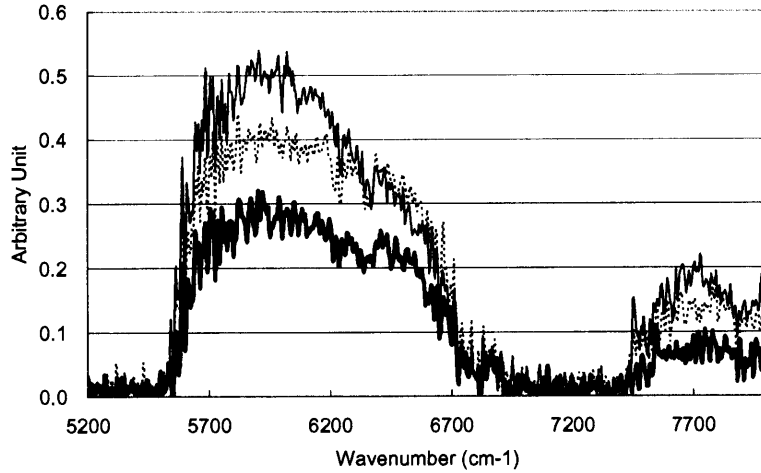


Figure 8-16. Incident angle dependency of the sea surface reflectivity in the case of refraction index of 1.33: parallel to the incident plane (doted line) and perpendicular to the incident plane (solid line).

**Measured spectra.** Figure 8-17 and Figure 8-18 show the level comparison between sun glint, skylight, and surface diffusive reflected light of the SWIR and visible (near infrared) spectra. The level of the diffusive or scattered light is about a few % of the specular reflection (sun glint). The results presented that the sun glint measurement had sufficient sensitivity to monitor CO<sub>2</sub> and CH<sub>4</sub> column amount. The optimization of the instrument parameters and improvement of the detector performance is need for diffusive reflection measurements.

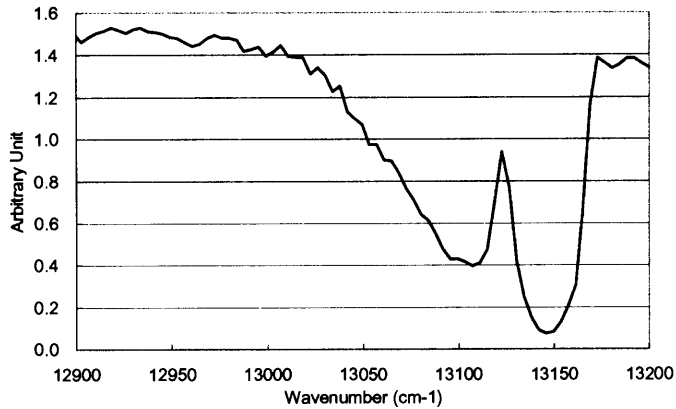


(a)

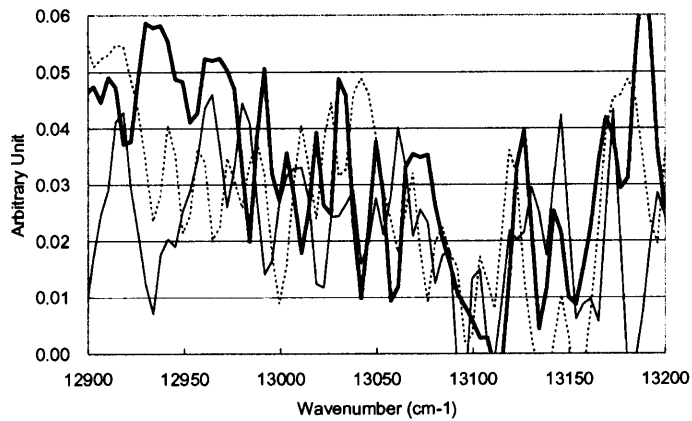


(b)

Figure 8-17. Radiance level comparison of SWIR region in Odawara on 6 December 2000 ( $8 \text{ cm}^{-1}$ ): (a) sun glint and at 11:10 am (b) skylight (dotted line), sea surface (scattering) (bold line), and land (forest)(solid line) at 11:19 am.



(a)



(b)

Figure 8-18. Radiance level comparison of visible region in Odawara on 6 December 2000 ( $8 \text{ cm}^{-1}$ ): (a) sun glint at 10:25 am and (b) skylight (dotted line), sea surface (bold line), and forest (solid line) at 10:30 am (1 shot).

**Optical path length estimation.** The simultaneously measuring wide spectra including O<sub>2</sub> absorption from 5200 to 8000 cm<sup>-1</sup> and from 12900 to 13200 cm<sup>-1</sup> are used to estimate the effective optical path length. The optical thickness can be retrieved as shown in Figure 8-19. O<sub>2</sub> is not interfered by H<sub>2</sub>O in visible spectra and fine absorption lines were measured clearly. In contrast, the accuracy of the aerosol effect correction is better since absorption in 7900 cm<sup>-1</sup> is close to the target spectral range of 5200 and 6400 cm<sup>-1</sup>.

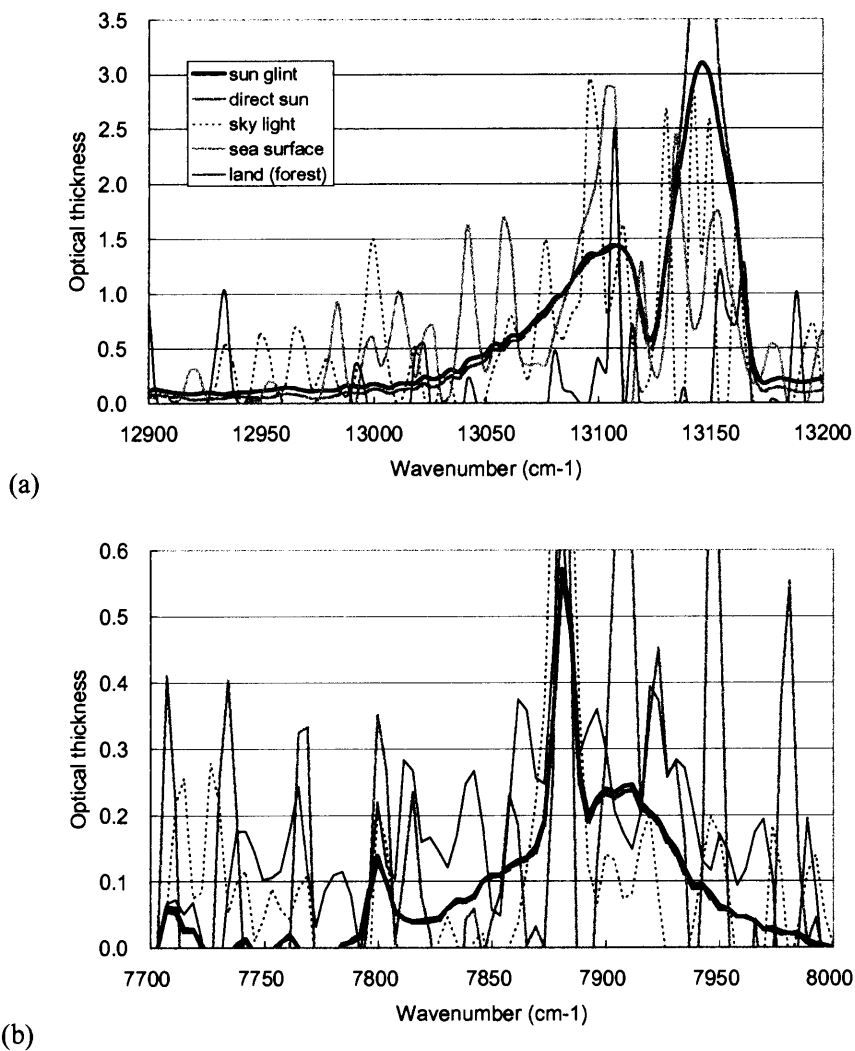


Figure 8-19. Measured optical thickness of O<sub>2</sub> absorption in (a) visible and (B) SWIR measured at 11:00 am in Odawara on 6 December 2000 with 8 cm<sup>-1</sup> resolution (1 shot)

**Sun glint measurements.** Figure 8-20 and Figure 8-21 show the measured spectra of CH<sub>4</sub> and O<sub>2</sub> together with the simulated spectra with radiative transfer models. The clear absorption spectra were acquired. In the satellite observation geometry, incident angle to the ocean surface is much smaller than ground observation. Figure 8-22 shows the measured sun-glint level at several different times together with the retrieved optical thickness of CO<sub>2</sub>, CH<sub>4</sub>, and O<sub>2</sub> from the measured SWIR spectra. As the results show, the

absolute levels of the radiance are not stable, but depend on the wind condition, in other words, the sea surface waveform. From these measured spectra, the optical thickness can be retrieved with absorption maxima and minima (differential absorption), in which case the retrieved optical thickness is uniform. Moreover, uniformity of the ratio of the CO<sub>2</sub> and CH<sub>4</sub> optical thickness to that of O<sub>2</sub> is improved by correcting the effective air-mass factor (optical path length).

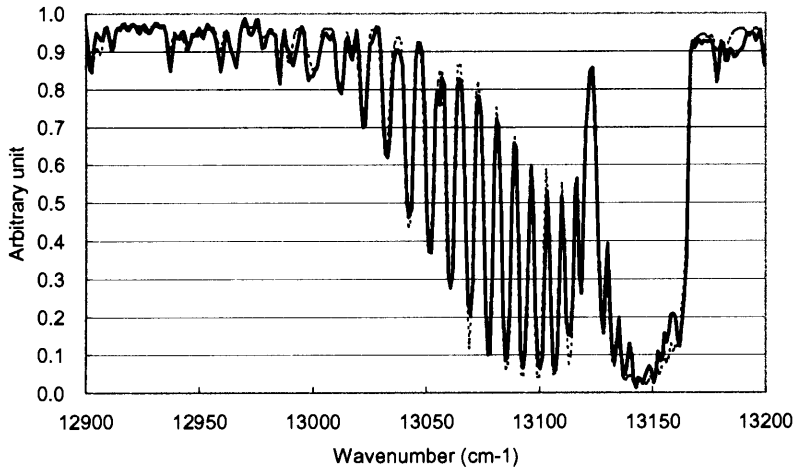


Figure 8-20. The measured spectra of O<sub>2</sub> with 2 cm<sup>-1</sup> resolution in Odawara on 6 December 2000 at 10:25 JST (solid line) together with the simulated spectra with radiative transfer models (dotted line).

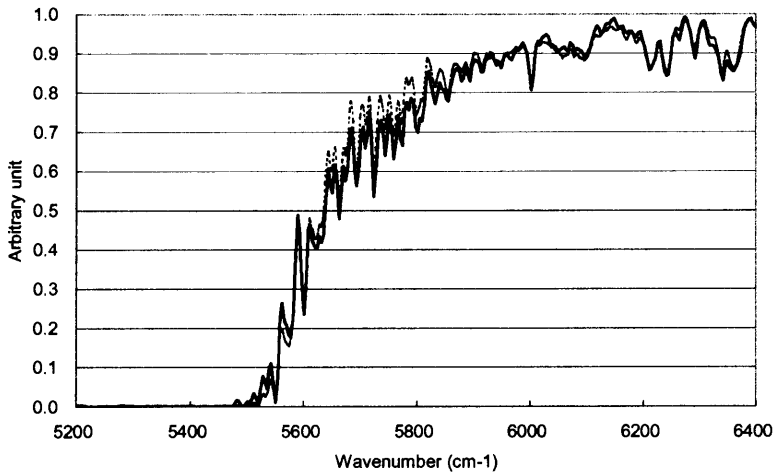


Figure 8-21 The same as Figure 8-20 except for 8 cm<sup>-1</sup> resolution and CH<sub>4</sub>.

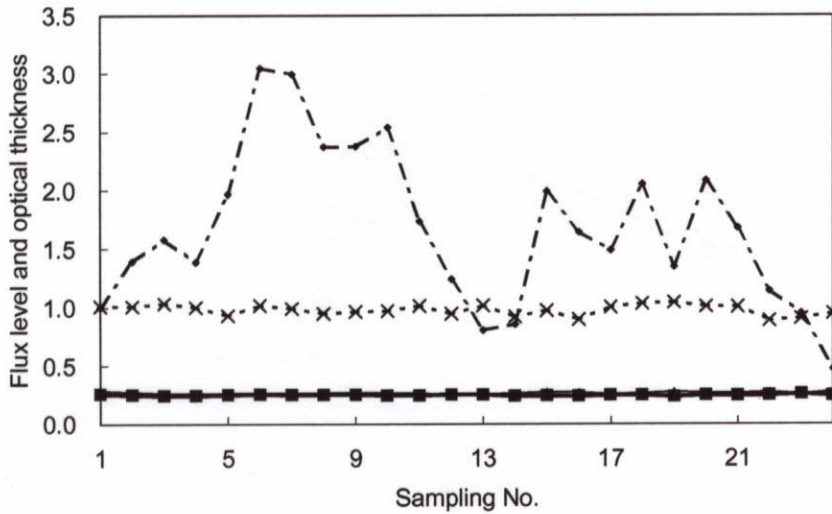
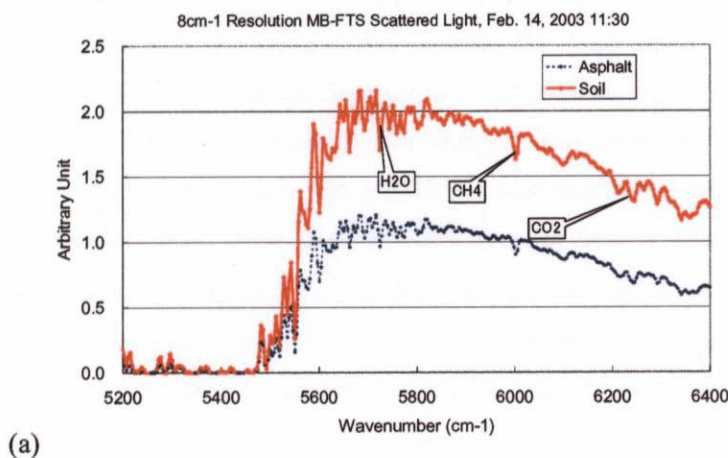
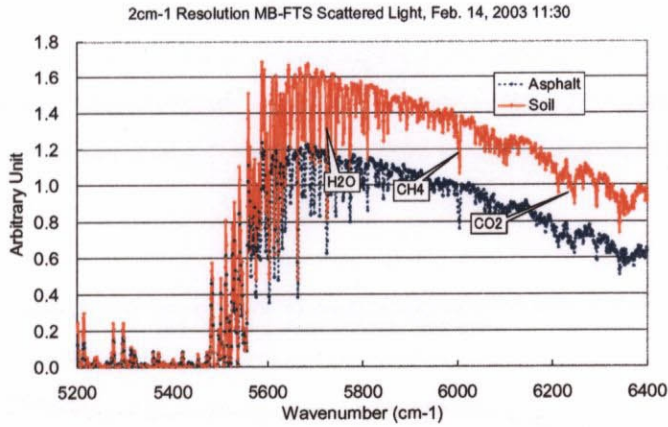


Figure 8-22. Sun-glint level variation (dash-dotted line) and optical thickness of CH<sub>4</sub> (bold line), CO<sub>2</sub> (solid line) and O<sub>2</sub> (dotted line) in Atami on 20 December, 2000 at 8:07 JST.

### (3) Ground-based test for demonstration of surface-scattered light measurements

Sun glitter can be observed over the ocean, where the atmosphere is less contaminated, and thus the observations over the land with the diffusive reflected light must also be considered. The typical diffusive surface albedo is about one-tenth of the sun glitter, and some kinds of land surface have spectral structures in the SWIR region. The spectral resolution and integration time must be carefully optimized to achieve a sufficient SNR and retrieve the target gases. The spectra reflected over the asphalt and soil under the clear sky conditions were measured as illustrated in Figure 8-23. Figure 8-24 depicts the relative surface albedo spectral structure derived from the measured data divided by the direct solar spectra. The result indicates that there are no fine spectral structures, such as molecular absorption. Therefore, the albedo spectral characteristics can be adequately corrected by measuring the back-ground level at both sides of the absorption.





(b)

Figure 8-23. Measured light scattered over the soil and asphalt surface with a MB160 FTS of (a)  $8\text{ cm}^{-1}$  and (b)  $2\text{ cm}^{-1}$  spectral resolution.

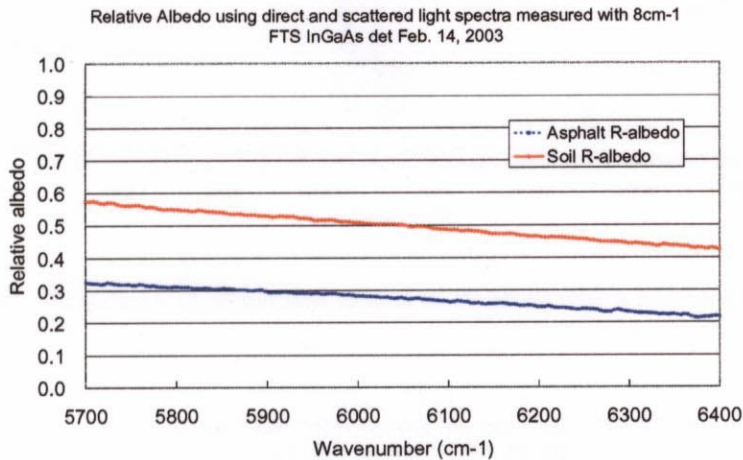


Figure 8-24. Relative spectral characteristics of the measured surface albedo of  $8\text{ cm}^{-1}$  spectral resolution..

#### (4) Characteristics of an imaging FTS tested in the laboratory

Imaging FTS technology using an array detector is a comprehensive method for space-borne applications to reduce the mechanical elements and increase the observation time. However, off-axis performance, such as wavelength shifts must be characterized. This technology is particularly useful for limb viewing observations. The off-axis performance was characterized under two conditions. Figure 8-25 presents the acquired  $\text{CO}_2$  absorption spectra with a 1770 K blackbody light source and 20-pixel PC MCT detector. These spectra were acquired simultaneously with a 20-pixel detector with a pitch of  $100\text{ }\mu\text{m}$ . The output levels of off-axis pixels are degraded since there are no fore-optics or pupil, but no significant degradation of the spectral resolution was observed at a  $32\text{ cm}^{-1}$  resolution. A fore-optics with a wide field lens and a collimator were introduced to investigate the off-axis effect in more detail. Figure 8-26 displays the acquired  $\text{CO}_2$  absorption spectra for a wide field of view of  $\pm 35$  degrees with a 1770 K blackbody light source, a wide field lens, and a PV MCT detector. These spectra were acquired by mechanically shifting the

single-pixel PV MCT detector. The input flux was collected in full by carefully aligning the optics and flux size. These data demonstrates the feasibility of an imaging FTS, although the wavelength shift due to the off-axis effect must be carefully characterized. The field of view is limited to about 1 degree, as in the limb scattering observation, which is about 50 km height from 3000 km away from the tangent point. Thus wide field optics are not necessary.

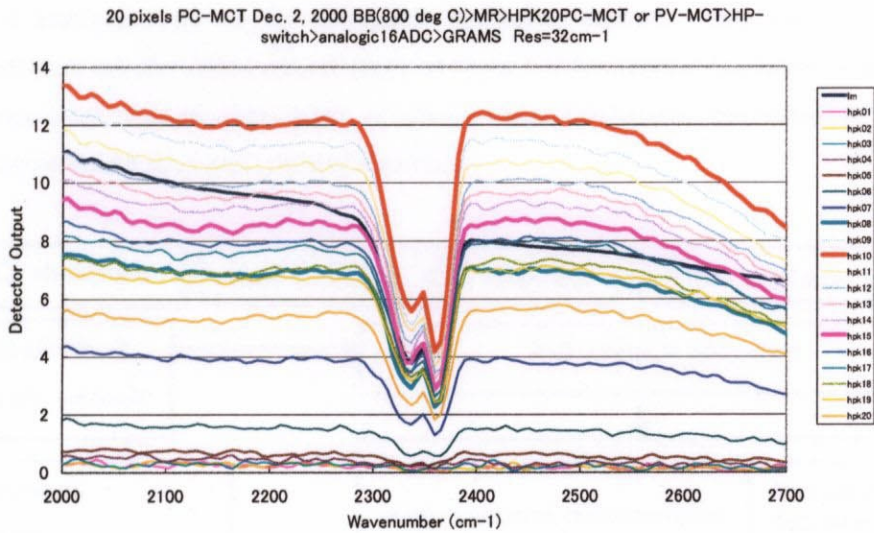


Figure 8-25. Acquired CO<sub>2</sub> absorption spectra of 20 pixels with a 1770 K blackbody light source.

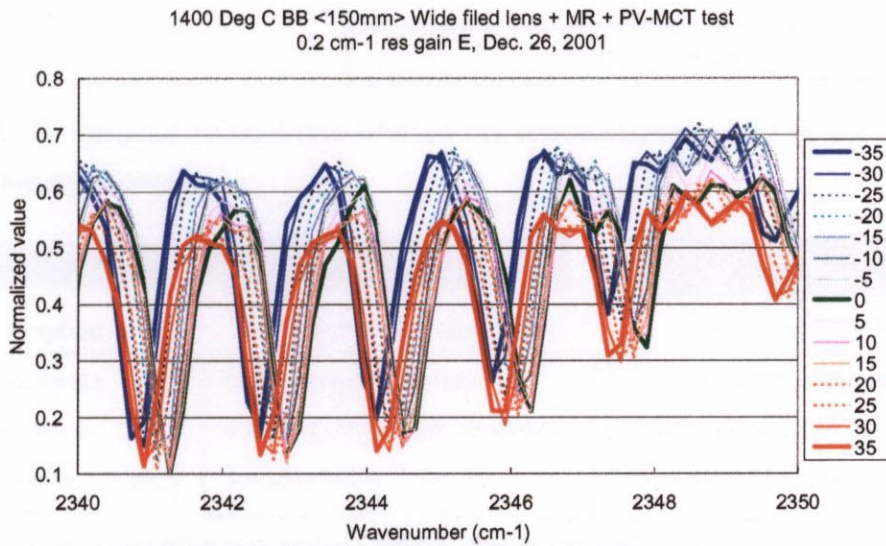


Figure 8-26. Acquired CO<sub>2</sub> absorption spectra for a wide field of view of +/- 35 degrees (5 degrees interval) with a 1770 K blackbody light source, a wide field lens, and a PV MCT detector.

## 8.6. Proposed Retrieval Algorithm for Column Density

The proposed retrieval algorithm of CO<sub>2</sub> and CH<sub>4</sub> column density was obtained as depicted in Figure 8-27 by applying the cloud and aerosol correction method for total O<sub>3</sub> retrieval for the SWIR nadir viewing measurements, spectral range of which is presented in Figure 8-28. Figure 8-29 indicates the MODTRAN refraction index model of typical aerosol in near IR and shortwave IR. There is no fine spectral structure and the differential absorption method will minimize the error due to aerosol interference. Figure 8-30 represents the transmittance and sensitivity of the differential absorption method. CO<sub>2</sub> and CH<sub>4</sub> have sufficient sensitivity as they have the absorption optical depth of about 1 if the spectral resolution is properly selected. The airplane observation over the thin clouds or aerosols and simultaneous acquisition of three bands are necessary to demonstrate the proposed retrieval algorithm

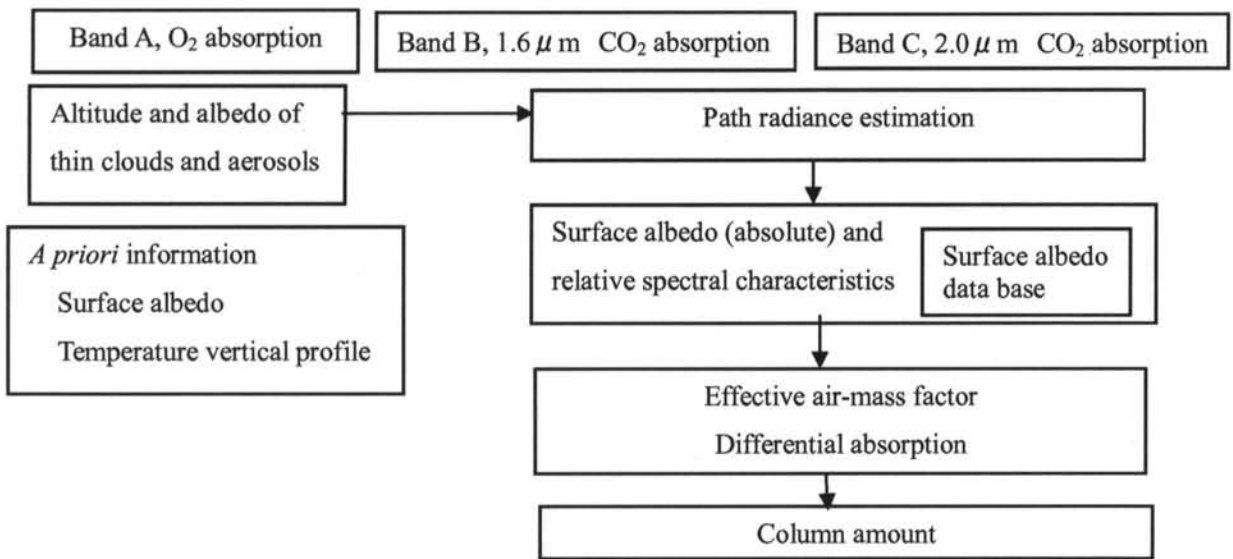


Figure 8-27. Proposed retrieval flow of cloud and aerosol correction for CO<sub>2</sub> and CH<sub>4</sub> column density retrieval.

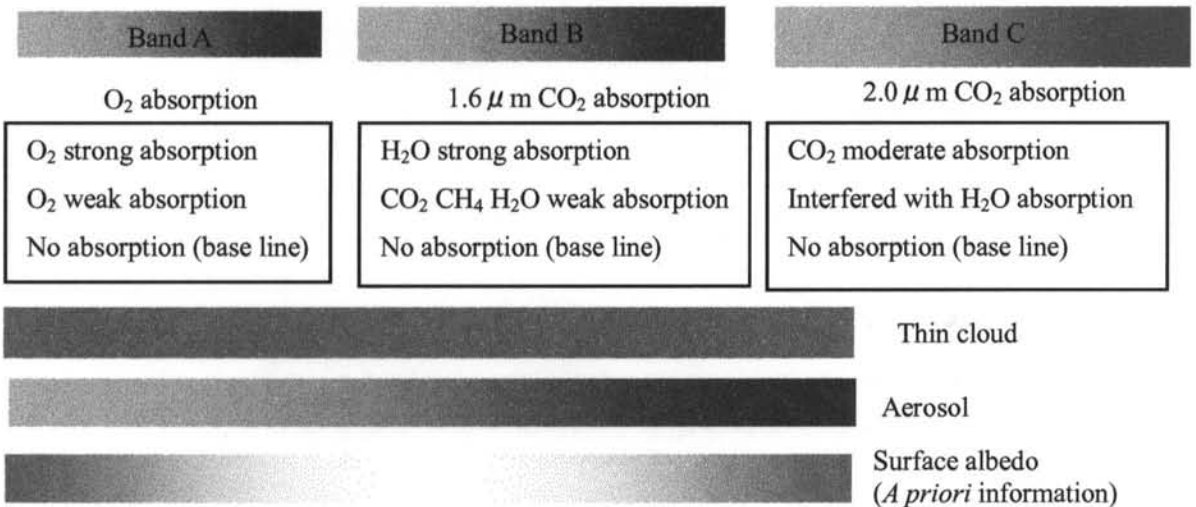
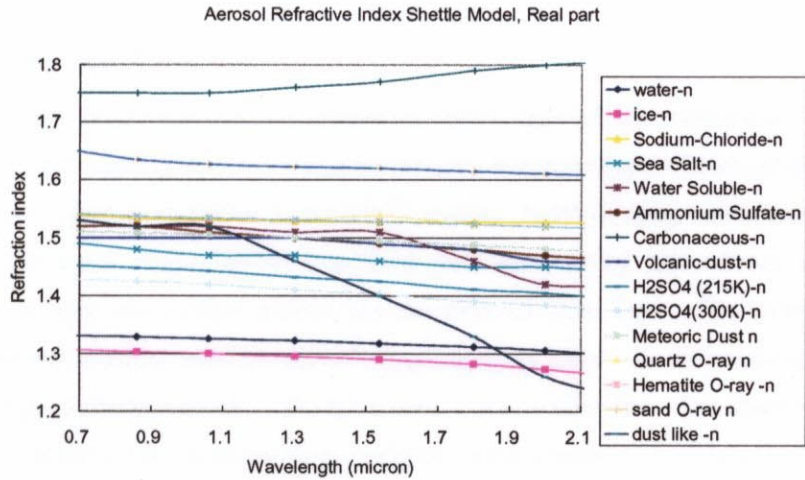
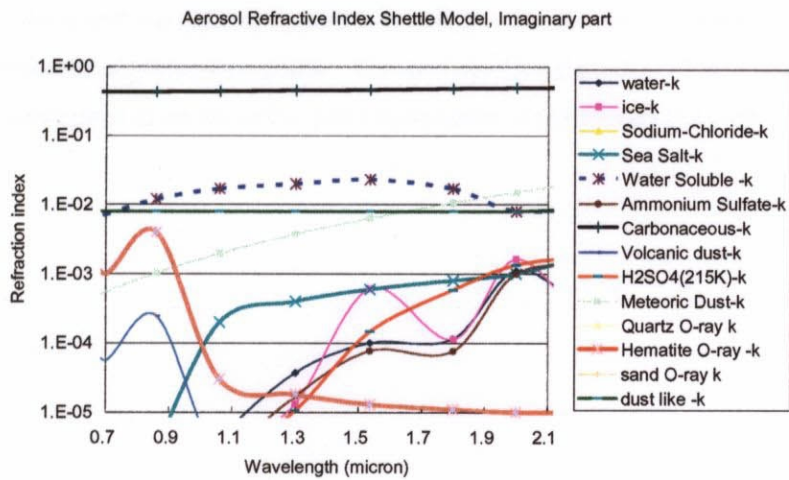


Figure 8-28. Spectral range used for CO<sub>2</sub> and CH<sub>4</sub> column density retrieval.



(a)



(b)

Figure 8-29. MODTRAN refractive index model of typical aerosol in near IR and shortwave IR: (a) real part and (b) imaginary part.

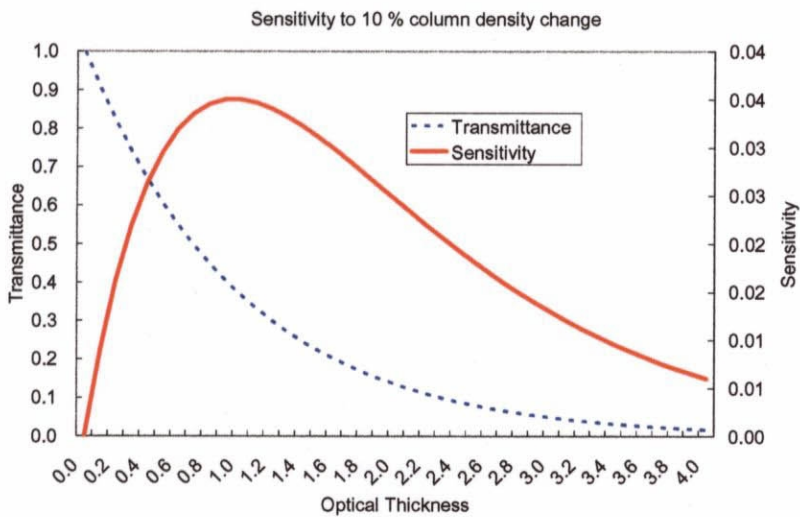


Figure 8-30. Transmittance and sensitivity of differential absorption method.

## 8.7. Conclusion of this Chapter

The laboratory model results and retrieval simulation with a mathematical model show the feasibility of limb-scattered light and nadir-looking sun glint measurements for monitoring greenhouse gases ( $\text{CO}_2$ ,  $\text{H}_2\text{O}$ , and  $\text{CH}_4$ ) globally with  $8 \text{ cm}^{-1}$  spectral resolution in the SWIR region. Nadir-looking measurements will provide the column amount with much higher spatial resolution than the existing space borne instruments. By observing limb-scattered light, the vertical profile can be retrieved from orbit. The contribution function represents the height resolution and it is calculated to be approximately 2 km. As scattered-light measurements use direct absorption, high vertical resolution with high accuracy can be expected. The absolute radiance of sun glint measurement itself depends on the sea surface condition (wind speeds etc.). The optical path and cloud interference can be properly corrected by measuring the  $\text{O}_2$  absorption spectra simultaneously. The combination of limb-looking and sun-glint measurements will provide accurate and frequent data of the global three-dimensional distribution of greenhouse gases. The data rejection algorithm of the cloud contamination or land surface must be investigated to optimize the data transmission to the ground from orbit.

## Chapter 9 Conclusion and Discussion

In this thesis, the data acquired with the existing instrument (TOMS) were first processed and the issues to be resolved were then extracted. The retrieval flow using the continuous UV and visible spectra, were then studied, the error was estimated, and the requirements for future instruments are presented here. An instrument that meets the specifications was then designed, manufactured, and tested. The conclusion of this thesis is summarized as follows.

**Information contents in the O<sub>2</sub> A band.** A rapid method to retrieve cloud top height and coverage was applied for GOME; the validation data verified the superior accuracy and precision of this method. The height and reflectivity of thin clouds and aerosols can be retrieved by improving spatial resolution. The aerosol height information will contribute to the classification of aerosol type.

**Tropospheric O<sub>3</sub> retrieval.** Total and (tropospheric) O<sub>3</sub> can be retrieved simultaneous with an accuracy of 3 DU (10 DU with a 5 km height resolution) using UV continuous spectra.

**Aerosol characteristics retrieval.** The surface albedos of both land and the ocean are low and carbonaceous and dust aerosols have absorption in the UV region. The aerosol type, height, and size information can be extracted using UV continuous data and O<sub>2</sub> A band data.

**Maximized optical throughput polychromator.** Superior optical throughput spectrometer was successfully developed using a combination of cylindrical mirrors and a custom-designed UV array detector. The diurnal variation of polluted NO<sub>2</sub> was measured on the ground using this spectrometer.

**Simultaneous atmospheric composition retrieval with single instrument.** The retrieval algorithm of atmospheric molecules, clouds, and aerosols with a single instrument will provide global and frequent data (daily) and contribute to our understanding of the chemistry and physics of the troposphere.

The objectives of the spectrometer development in this thesis were to study the optimized design of high-spectral-resolution spectrometers, their characterization, calibration, and retrieval algorithm using the data acquired with those spectrometers. The limitations of the resources and observation time in orbit make it impossible to achieve sufficiently high spectral resolution to observe the absorption line shape, which has a bandwidth of less than 0.1 cm<sup>-1</sup>. However, a moderate resolution spectrometer has sufficient sensitivity to detect atmospheric constituents if the instrument function is well characterized and the absorption spectra are accurately simulated. Therefore, the spectral resolution must be optimized to maximize the signal-to-noise ratio (SNR). Existing instruments have limited spatial and spectral resolution and limited spectral channels; they only measure the first order of geophysical parameters that govern radiative transfer in the atmosphere, such as the total column amount and surface albedo. The newly designed instrument and newly developed algorithm described in this thesis enable retrieval of the second order of geophysical parameters, such as tropospheric O<sub>3</sub>, aerosol, and minor constituents. These retrieved parameters not only provide scientific data on the radiation budget and air pollution, but also improve model simulation accuracy. In addition, the retrieval accuracy of first-order parameters, such as total O<sub>3</sub> retrieval, is also improved. A combination of improved instruments and the retrieval algorithm will provide better understanding of the Earth's atmosphere.

## 9.1. Retrieval Algorithm -Tropospheric Measurements from Space

The spectrometers described in this thesis will provide high SNR and moderate spectral resolution spectra of a wide spectral coverage by introducing new electro-optical technologies and using an instrument function characterization method as illustrated in Figure 9-1. The highly accurate data from these instruments provide the potential to retrieve new geophysical parameters from space.

Atmospheric constituent retrieval using continuous spectral data enables us to solve the equations of spectral channels. Measured spectra that are weak absorption of atmospheric molecules become a linear equation. However, the actual measured spectra are combination of cloud interference and weak and strong absorption of molecules and aerosols. Therefore, they are not expressed as linear equations; each geophysical parameter has different sensitivity in the measured data. The retrieval algorithm must be carefully tuned. In addition, the actual measurement data include random and systematic errors. Optical thickness must therefore be analyzed. However, the measured value of the transmittance and dynamic range of satellite-borne measurements is limited. The absorption strength used for retrieval must be carefully selected. Rapid data processing in quasi-real time is also required.

Frequent observation and high spatial resolution are required to monitor tropospheric compositions, particularly urban area air-pollution, and biomass burning. Lower tropospheric measurements from space are generally difficult due to interference from the upper atmosphere (upper troposphere and stratosphere) and clouds. Cloud detection, surface albedo, and aerosol optical thickness, tropospheric O<sub>3</sub> retrieval and greenhouse gases total column and vertical distribution monitoring are studied for this thesis. The detection algorithm of cloud height and coverage, which often interferes with troposphere measurements, is presented in Chapter 3. This method is now used as an operational algorithm for ERS2 GOME cloud detection. This thesis presented a simultaneous retrieval algorithm for atmospheric molecules, radiation budget, clouds and aerosols with a single instrument, primarily using wide spectral region in Chapter 4. The algorithm is basically the grid search method and is suitable for processing a large amount of data in quasi-real time. Figure 9-2 illustrates summary of the increased retrieved parameters using UV and visible continuous spectral measurement from space.

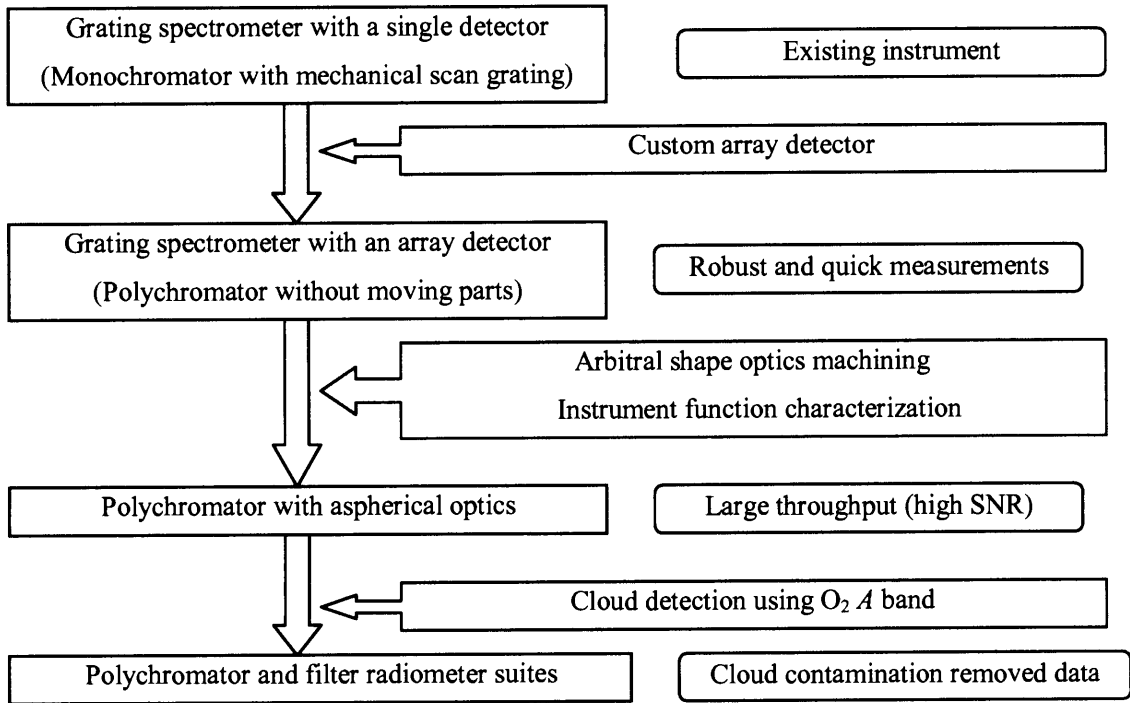


Figure 9-1. Performance improvement of the instruments and newly retrieved geophysical parameters described in this thesis.

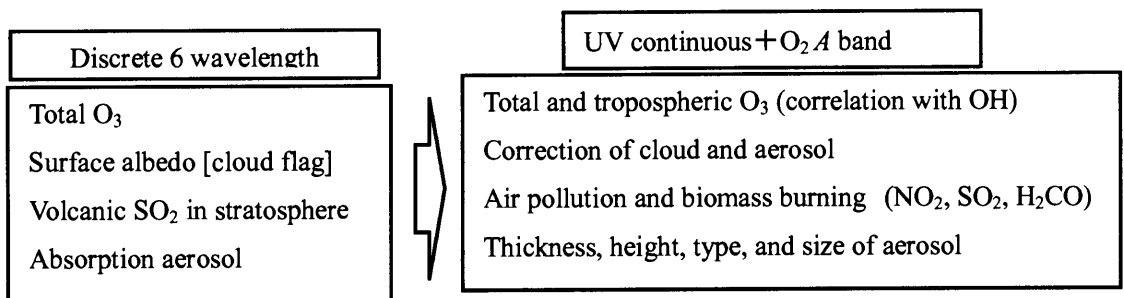


Figure 9-2. Summary of the increased retrieved parameters using the UV and visible continuous spectral measurement from space.

## 9.2. Improved Instrumentation and Expected Science

Recent improvements in the optics and detector technology will contribute to advances in observations from space. Recent manufacturing improvements using numerically controlled cutting tools have introduced arbitrarily-shaped aspherical mirrors with sufficient surface quality for spectrometer application. Custom-designed array detectors with an amplifier and readout electronics on a single chip can be optimized for spectroscopic observations. In addition, the optical performance (ray tracing and refraction) and detector capability have been well modeled and simulated. The spectral radiance of the input flux has been well simulated using a radiative transfer model with molecular, aerosol, and solar irradiance databases. The performance of the spectrometer has been improved and well characterized by combining the new technology,

model calculations, and ground-based test. Compactness (weight and size), speed (rapid measurements), and robustness of the instruments are necessary for space applications in addition to the electro-optical performance. The designs of three grating spectrometers (UV polychromator, ILAS balloon-borne polychromator, and ILAS-II echelle-grating polychromator), one filter radiometer (cloud-detection radiometer), and two FTSs (solar occultation FTS and SWIR FTS for future application) are discussed in this thesis. The optimized designs of the instruments are summarized as below.

### **(1) High SNR grating polychromator system and slit function characterization**

Moderate spectral resolution is required for UV and visible regions to obtain sufficient sensitivity to detect minor constituents. The grating spectrometer is the optimal device to meet this requirement as discussed in Chapter 5. Simultaneous data acquisition, achieved through polychromator design, is required for space applications to optimize the integration time and eliminate moving parts. Recent array-detector technology and aspherical-optics technology, both simulated and manufactured, have produced a wide spectral range polychromator that corrects the astigmatic aberration. The polychromator, manufactured as an engineering model, has a uniform Gaussian shape instrument function over the entire spectral range and has very small wavelength shift due to the thermal distortion on orbit. These characteristics offer significant advantages, particularly for differential absorption spectra measurements and the look up table method to save calibration, tuning, and computation time. It also collects most of the spread light in the focus due to the astigmatic aberration without degrading the spectral resolution or increasing the detector noise. The results of the ADEOS TOMS  $O_3$  demonstrated the importance of characterizing the instrument function to determine the effective center wavelength. The retrieved data was not self-consistent and had to be tuned using ground and sonde validation data since the existing TOMS algorithm does not consider the slit function characteristics. The total  $O_3$  can be consistently retrieved without using the correction factor by calculating the radiative transfer at five wavelength points in each channel, taking into account the weight of the instrument function.

Modification of the visible spectrometer of ILAS for balloon validation was discussed in Chapter 3. A moderate SNR and high spectral resolution can be achieved simultaneously by replacement with a fine-pitch 1D array CCD detector with 5000 pixels, a width of  $7\ \mu\text{m}$ , and a rectangular shape slit, which compensates for image degradation due to astigmatic aberration,

An echelle-grating spectrometer, which has significant dispersion compared with a regular grating, can achieve  $0.1\ \text{cm}^{-1}$  spectral resolution, as described in Chapter 6. The combination of rectangular slit, aspherical mirror collimator, and two aspherical cylindrical collecting mirrors can provide optimized spectral resolution and spatial resolution for solar occultation with a SNR. Therefore, the small amount of  $\text{ClONO}_2$  in the polar region can be detected with this compact grating spectrometer with a 1 km vertical resolution. A compact grating spectrometer is an optimal apparatus since the observation of ILAS-II is limited to the polar region  $O_3$  chemistry and one molecule. In contrast, the IR FTS for solar occultation measurement is for both  $O_3$  chemistry and global greenhouse gases measurements, and many molecules can be measured.

A characterization of the instrument function using a monochromatic light source and model calculation using an optical performance simulator were presented in this thesis, and their results agree. In addition, the

data of the ground observation coincides well with the convoluted value of the instrument function and simulated spectra produced by the radiative transfer model. These results demonstrate that the applicability of the moderate spectral resolution remote sensing. Accurate characterization of the slit function and high SNR are important than spectral resolution since heavy molecules have moderately wide absorption lines and most of the atmospheric molecules have many adjacent lines. However, some diatomic molecules, such as NO and HCl, require very high spectral resolution.

## **(2) Cloud contamination removal with a filter radiometer**

A filter radiometer is the conventional method for absorption spectra measurements when only one of two physical parameters are to be retrieved. A grating polychromator is sensitive to the thermal distortion onboard and the information contents are limited to the effective optical path in cloud detection applications using the visible  $O_2 A$  band spectra, as discussed in Chapter 3 and Chapter 4. A filter radiometer is robust and suitable for cloud detection using  $O_2 A$  band since  $O_3$  and  $H_2O$  absorption is negligible and the line width of  $O_2$  absorption is moderately wide.

## **(3) Compact rapid-scan Fourier-transform spectrometer for solar occultation application**

Fourier-transform spectrometer (FTS), which covers a wide spectral range, is the most comprehensive apparatus for infrared spectroscopy. The instrument can be designed to be compact if the required spectral resolution is moderate and the time constant is small enough for space applications. Two applications are discussed in this thesis: solar occultation in thermal infrared and sun-glint measurements in shortwave infrared.

FTS has two advantages, the multiplex and throughput advantage. The multiplex advantage is applied for both solar occultation and sun-glint measurements. This advantage enables wide spectral range measurements with a single detector. The throughput advantage is applied for nadir-looking measurements. The SNR and spectral resolution can be optimized using FTS since the spatial scale of the atmospheric constituents is relatively large. However, the time constant is short for space-borne measurements and rapid scanning and data acquisition are required. This thesis describes the feasibility of a space-borne FTS with a double-pass configuration, feed-forward control of the moving mechanism, and 200 KHz 16 bit AD conversion.

## **(4) Simultaneous measurements of temperature and pressure vertical profile by a grating spectrometer**

Solar occultation is a comprehensive method for atmosphere molecular spectroscopy. The light source of the Sun is sufficiently bright to achieve high spectral resolution, and the absorption spectra of each molecule are thus well separated. This method measures absorption directly. The pressure level estimation error of the tangent point and the absorption intensity constant error due to estimated temperature uncertainty are the primary error sources when the absorption cross section has strong temperature dependency. A grating spectrometer measures the  $O_2 A$  band spectra by observing the same field of view to minimize the error. This thesis describes use of the moderate spectral resolution of an  $O_2 A$  band grating polychromator to achieve

robust onboard performance.

### (5) Optimized selection of SNR, spectral and spatial resolution, and frequency

Table 9-1 lists the key instrument parameters of space-borne spectrometers for atmospheric observations using different methods. The theoretical limit of the achieved SNR can be estimated using the following equation assuming detector noise is the dominant noise source.

$$SNR = \frac{D^* L A_c \Omega_c \Delta \nu \eta}{A_d^{1/2} \Delta f^{1/2}}, \quad (9-1)$$

where  $D^*$  represents the specific detectivity;  $L$ , the spectral radiance;  $A_c \Omega_c$ , the optical throughput;  $\Delta \nu$  spectral bandwidth;  $\eta$ , the optical efficiency;  $A_d$ , detector area; and  $\Delta f$ , electrical bandwidth. The simple calculation provides that in the limb-viewing measurements except for solar occultation SNR is low at the expense of vertical spatial resolution. The actual instrument has additional noise from jitter of FTS moving mechanism, shot noise of the signal and dark currents, and switching noise. Therefore, the maximum SNR that can be achieved on orbit with passive remote sensing is on the order of 1000. The recent need to measure the total column amount of greenhouse gases requires high spatial resolution and high SNR for monitoring purposes. Needle-point measurements are feasible by active remote sensing such as LIDAR, which requires resources and considerable expense for space application. Remote sensing is the trade-off between the spatial and spectral resolution and SNR. Therefore, a light source with very strong radiance is needed to achieve needle-pointing measurements. Solar occultation can achieve the very high spectral and vertical spatial resolution, but the horizontal spatial resolution is low. Only Sun-glint measurements can enable needle-point measurements of the total column amount with a very high SNR, as indicated in Table 9-1.

Table 9-2 provides the typical parameters of ultraviolet, visible, shortwave, and thermal infrared spectroscopy. Only UV and visible spectroscopic measurements can achieve global coverage within one day, as schematically illustration in Figure 9-3. These characteristics are particularly important for troposphere observations, for which the time and spatial scale are much smaller than those for stratospheric measurements. In addition, established silicon detectors and read-out technologies can be used for UV and visible spectrometers without cryogenics.

Table 9-1. Key instrument parameters of space-borne spectrometers for different atmospheric observations.

	Instrument example	Wavelength (typical)	Light source color temperature	Light source	Surface Albedo or Emissivity	Spectral radiance	Spectral radiance	Detectivity D*	Aperture	Spatial resolution at the target	Spatial resolution	Optical Throughput	Detector size	Optical efficiency	Spectral resolution	Time constant	Expected SNR (simplified model)	
		μm	K	-	-	W/cm2/str/cm-1	W/m2/str/micron	cmHz1/2W-1	cm	km	rad	cm2str	cm	-	cm-1	s		
UV	Nadir scattering	OPUS	0.32	5900	Scattered light*albedo	0.2	5.6E-06	55	5.0E+12	0.36	20	3.1E-02	9.6E-05	0.052	0.3	49.00	0.03	1333
V	Nadir scattering	OPUS	0.76	5900	Scattered light*albedo	0.2	3.6E-07	63	5.0E+12	0.23	4	6.2E-03	1.6E-06	0.002	0.3	10.00	0.03	686
V	Nadir-Scattering	FTS	0.76	5900	Scattered light*albedo	0.2	3.6E-07	63	5.0E+12	5.00	8	1.2E-02	2.3E-03	0.100	0.1	1.00	0.50	2995
SWIR	Nadir scattering	FTS	1.57	5900	Scattered light*albedo	0.2	2.6E-07	11	1.0E+12	5.00	8	1.2E-02	2.3E-03	0.100	0.1	0.50	0.50	217
SWIR	Sun glitter	FTS	1.57	5900	Scattered light*albedo	9.0	1.2E-05	479	1.0E+12	1.00	8	1.2E-02	9.3E-05	0.020	0.1	0.50	0.20	1233
SWIR	Limb scattering	FTS	1.57	5900	Scattered light*albedo	0.1	1.3E-07	5	1.0E+12	10.00	1	3.4E-04	7.1E-06	0.015	0.1	10.00	10.00	196
IR	Nadir emission	IMG	10	260	Blackbody	1.0	4.7E-06	5	2.0E+11	10.00	10	1.3E-02	9.6E-03	0.200	0.1	0.05	10.00	719
IR	Nadir emission	EarthCAR E FTS	15	260	Blackbody	1.0	9.0E-06	4	2.0E+11	3.00	10	2.2E-02	2.7E-03	0.150	0.1	0.50	1.20	1811
Solar Occultation		SOFIS	10	5900	Blackbody	1.0	4.3E-03	4317	2.0E+11	6.00	1	3.4E-04	2.6E-06	0.010	0.1	0.20	0.20	1970
IR	Limb emission	-	10	260	Blackbody	1.0	4.7E-06	5	2.0E+11	10.00	1	3.4E-04	7.1E-06	0.015	0.1	0.50	10.00	71

Table 9-2. The typical parameters of the ultraviolet, visible, shortwave, and thermal infrared spectroscopy.

	$\Delta\nu$ cm <sup>-1</sup>	D* Cm Hz <sup>1/2</sup> W <sup>-1</sup>	L W/str/cm <sup>2</sup> /cm <sup>-1</sup>
Ultra violet, Visible	5	5e12	9e-8
Short Wave Infrared	0.5	4e11	4e-7
Thermal infrared	0.1	2e11	5e-6

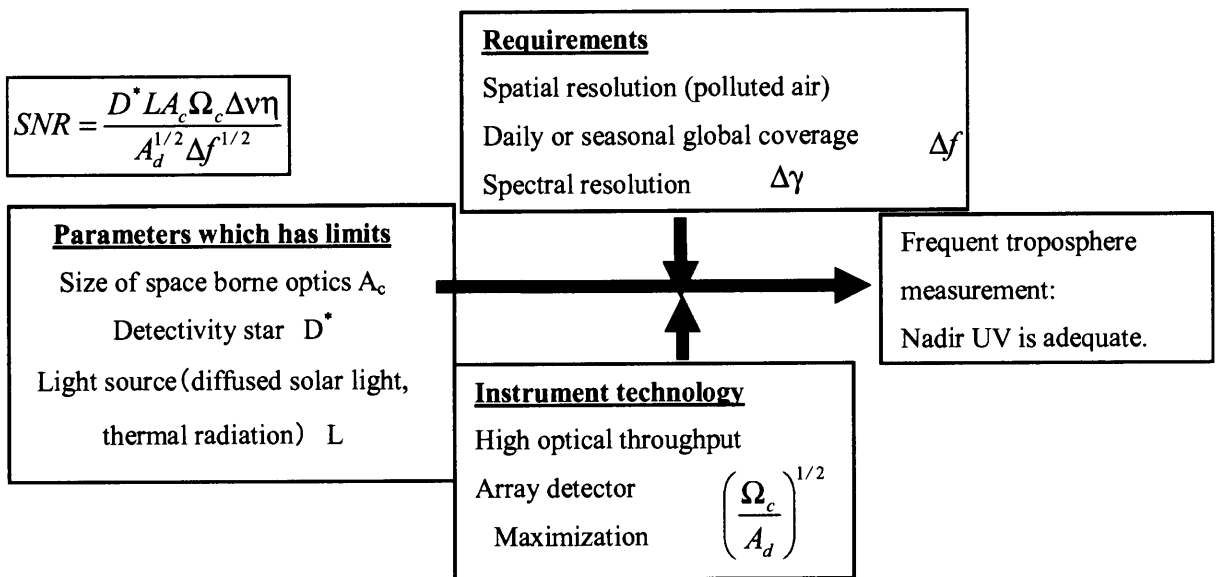


Figure 9-3. Advantage of UV nadir remote sensing for frequent and moderate spatial resolution.

## (6) Trade off between a grating polychromator and Fourier transform spectrometer

Both the grating spectrometer and Fourier transform spectrometer are widely used and the trade-offs between two methods are summarized in Table 9-3. The spectral resolution of an as-manufactured grating spectrometer can be tuned by changing the entrance slit width, and the spectral range can be selected by replacing the grating and detector. The spectral resolution of an as-manufactured FTS can be selected by tuning the scanner traveling distance and the spectral region can be selected by replacing the beam splitter and the detector. Thus, both a grating polychromator and an FTS can be applied for satellite borne measurements from UV to thermal infrared. The grating polychromator is recommended when imaging capability and short-period global coverage are required. In contrast, the FTS has advantages when high spectral resolution and weak light detection are necessary.

Table 9-3. Summary of the comparison between grating polychromator and Fourier transform spectrometer.

	Grating polychromator	Fourier transform spectrometer
Spectral resolution	Up to $0.1 \text{ cm}^{-1}$	Up to $0.01 \text{ cm}^{-1}$
Maximum number of channels	Up to about 1000 (Limited by number of pixels of array detector)	Up to 10000
Data acquisition	Electrical scanning, faster than 1 msec	Mechanical scanning and mechanical turnaround, at least 30 msec is needed.
Optical throughput		
Speed of the optics	F=1 (limited spectral range) F=3.5 (wide spectral range)	Up to F=1
IFOV	Determined by the array detector manufacturing feasibility	Obliquity limit (determined by the resolution power)
Noise source	Detector noise	Detector noise, sampling jitter, quantum noise
Data processing	Simple	Fourier transform (correction such as phase delay is needed.)
Reliability, fidelity	High Uniform shape of slit function	Mechanical scan is needed Uniform shape of slit function

## 9.3. End-to-End Research and Development

Remote sensing from space is an integrated system of onboard and ground components that includes instrumentation and a retrieval algorithm. Spaceborne instruments can provide data with minimal relative-error since the space environment is stable during a satellite mission. Any efficiency decrease can be assumed to be linear if the degradation due to contamination, high-energy radiation, UV radiation, and atomic

oxygen exists. Therefore, the validation by ground, airborne, and balloon measurements is important to minimize systematic error. Retrieval algorithm for nadir-looking measurements must use *a priori* vertical profile information, since the measured data will have random and systematic errors and height resolution is limited. The accuracy of the absorption cross section and its temperature dependency, which must be precisely measured in the laboratory, are important as well when retrieving the column amount from the absorption spectra. Figure 9-4 schematically illustrates the concept of end-to-end instrument and algorithm development. Satisfactory measurements can be achieved only when suitable instrument design, algorithm, validation, calibration, and laboratory measurements are achieved.

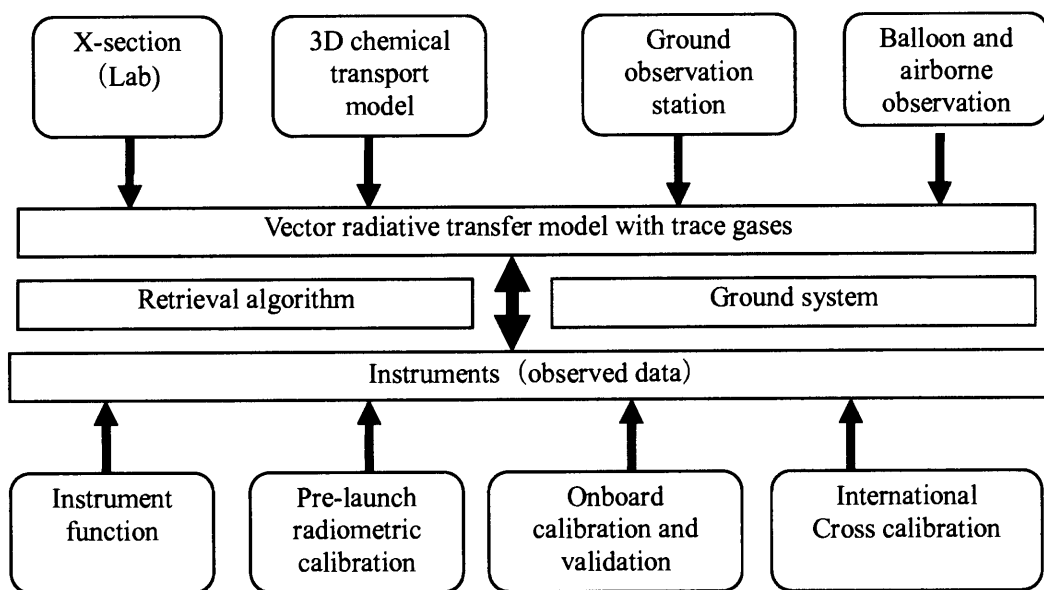


Figure 9-4. Concept of the end-to-end instrument and algorithm development.

### 9.4. Instruments for Future Application

This thesis describes the designs of both the grating spectrometer and Fourier-transform spectrometer, which achieves  $0.1 \text{ cm}^{-1}$  resolution and is suitable for IR remote sensing, as schematically illustrated in Figure 9-5. A retrieval algorithm to improve troposphere measurements was also studied. A new observation method to monitor greenhouse gases columns was proposed. The physics of the troposphere are complicated compared with the stratosphere, and the time scale is short because it is affected by convection, human activity, water circulation, and interaction between the ocean and land. Therefore, more frequent and accurate measurements from space are needed. An SWIR FTS with a rapid-scan mechanism and multiple pixels is a feasible method to meet these requirements.

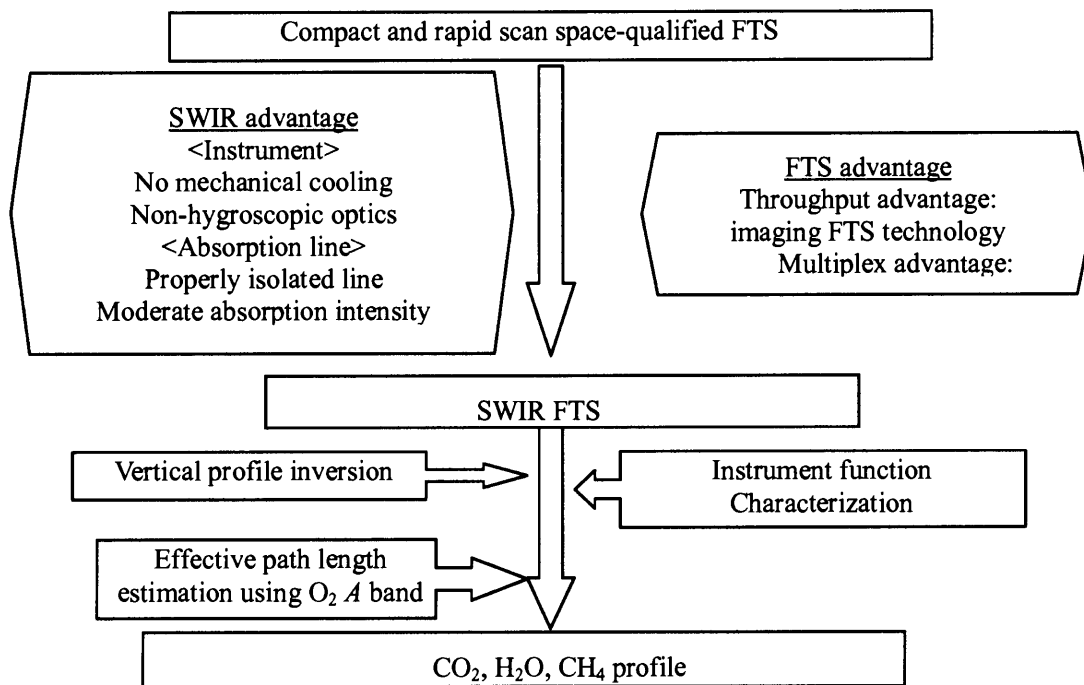


Figure 9-5. Proposed SWIR-FTS instrument and algorithm for future application.

## 9.5. Expected Scientific Output in the Present and Future Missions

The information acquired from satellite data will be greatly enhanced by improving the SNR of existing satellite-borne instruments and characterizing the spectral response (instrument function). Figure 9-6 depicts the data products and expected scientific output from the newly developed instruments and retrieval algorithm in this thesis.

A-UV polychromator achieves an extremely high SNR and a slit function with high fidelity by utilizing moderate spectral and spatial resolutions. It also can monitor polluted air ( $\text{NO}_2$ ,  $\text{SO}_2$ , and carbonaceous aerosols from urban areas;  $\text{O}_3$  from biomass burning; and dust from desert area) and is able to provide the dynamics of these compositions using global coverage data from one day. The ILAS-II echelle-grating spectrometer has a high spectral resolution at  $12.8 \mu\text{m}$  to detect the  $\text{ClONO}_2$  vertical profile. It provides data from about 30 occultation events in one day. This frequent data will reveal the polar region  $\text{O}_3$  depletion and recovery mechanism in the stratosphere.

Detection of the sources and sinks of  $\text{CO}_2$ , which contributes most to the global warming, is important for climate-change monitoring. They can only be retrieved by inversion method using a chemical transport model. There are presently a limited number of ground stations that monitor the background level of  $\text{CO}_2$  density and provide monitoring data (constraint). There are a limited number of stations in tropical regions, and thus the inverted source and sink data includes uncertainties and the spatial resolution is presently very low. A solar occultation FTS will provide global data that includes high latitudes that shuttle-born ATMOS cannot cover. It can measure most of the major and key constituents, such as reservoir ( $\text{ClONO}_2$  and  $\text{HCl}$ ) to clarify the upper troposphere and stratosphere chemistry. However, uncertainties in the vertical distribution model in the lower troposphere and chemical transport model remain. The spatial resolution is limited due to the

nature of the inversion, and it is difficult to identify the sources and sinks of certain area such as megalopolises. SWIR FTS measurements, which combine of the total column measurement using sun glint and diffused reflection light over land and a vertical profile measurement using the light scattered by the atmosphere, will provide more accurate data in future missions with grater spatial resolution than the existing methods, such as solar occultation and thermal radiation from the nadir. This instrument may also provide the potential for directly measuring sources and sinks of greenhouse gases.

The relations between improvements of the instrumentation and retrieval algorithm and the scientific output from the improvements described in this thesis are summarized and illustrated in Figure 9-7.

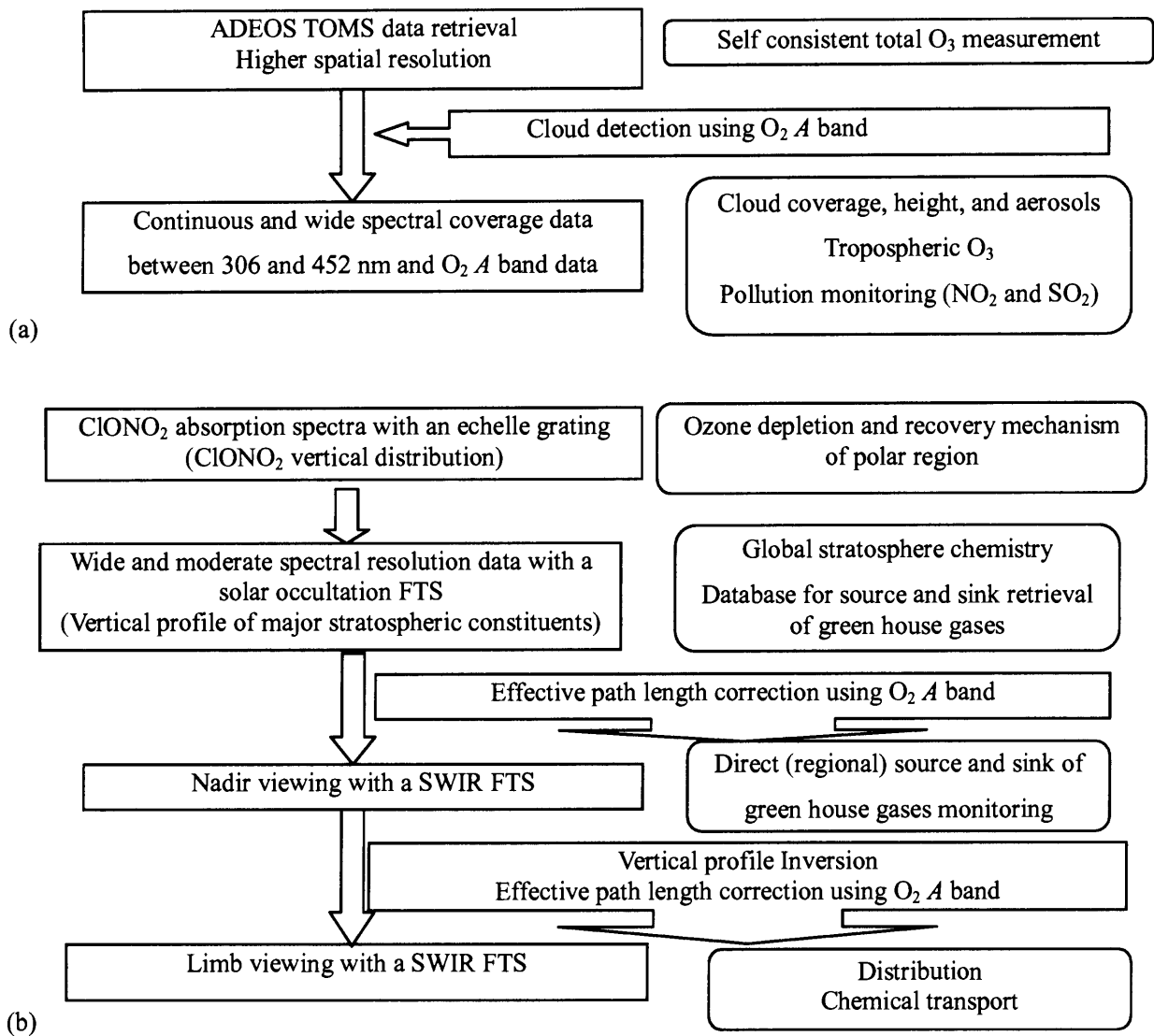


Figure 9-6. Data products and expected scientific output from the newly developed instruments and retrieval algorithm in this thesis. (a) UV and V remote sensing and (b) IR remote sensing.

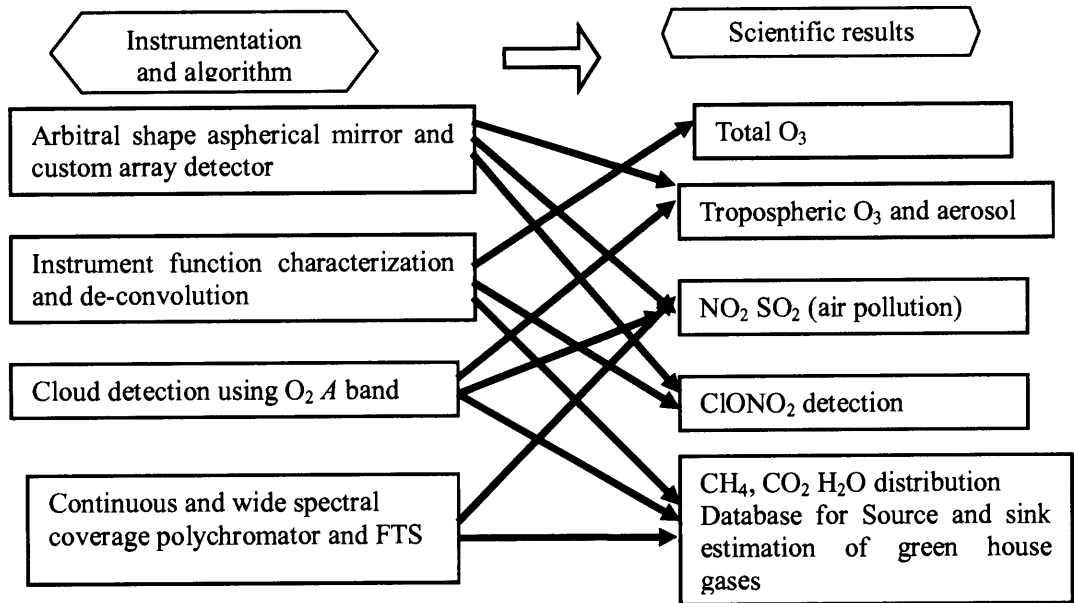


Figure 9-7. The relations between the improvements of the instrumentation and retrieval algorithm and the scientific output from these improvements in this thesis.

Today, Earth's environment is presently the most important issue for humans to address. Remote sensing from space is a very powerful tool for observing and monitoring Earth's atmosphere. Tropospheric atmospheric composition measurements in particular are crucial. Clouds and aerosols must also be detected; existing instruments have limited SNR and spectral resolution performance. Accurate and detailed physical and chemical parameters of the Earth's atmosphere were investigated here by introducing newly developed technology, instrument characterization techniques, and a retrieval algorithm. The results of this thesis will contribute not only to solutions for environment issues but also to a better understanding of the natural phenomena.

## Acknowledgements

The author wishes to express special thanks to Naomoto Iwagami, Teruyuki Nakajima, Yutaka Kondo, Makoto Koike, and Ryoichi Imasu of University of Tokyo, Kelly V. Chance of the Harvard Smithsonian Center for Astrophysics, Yasuhiro Sasano and Hideaki Nakajima of National Institute for Environmental Studies, Toshihiro Ogawa, Makoto Suzuki, and Hirokazu Yamamoto of NASDA Earth Observation Research Center, Seiichi Sasaki of NEC Aerospace Systems Ltd., and Shigetaka Mori, Takahiro Kawashima, and Jun Tanii of NEC Toshiba Space Systems Ltd., and OPUS sensor team. The author thanks Teruyuki Nakajima of University of Tokyo for providing the STAR code, Arlin Krueger of NASA GSFC and Glen Jaross of Raytheon (former Hughes) STX Corporation for helpful information on TOMS, Takakiyo Nakazawa of Tohoku University for providing a Bomem DA2 interferometer. The author also wish to express thanks to Norio Kimura, Katsunori Waragai, and Nobuhiro Araki of Matsushita Communication Industrial Co., LTD., Seiichiro Mizuno of Hamamatsu Photonics K.K., Seiji Toyama of Fuji Photo Optics Co., Marc-Andre Soucy of ABB-BOMEM Inc., Heater Wickman of BAE systems, Nobuyuki Uemura of Fujitsu FIP Co. and Atsushi Takeuchi of Nippon Avionics Co. LTD. for their technical discussions. The cloud detection study of this research was supported by NASA Grant NAGW-2541. They also thank Shinichi Nagata of the Ministry of the Environment for funding SOFIS program.

## References

- Aoki, T., M. Fukabori, and T. Aoki, Optical remote sensing of greenhouse gases in the troposphere, *SPIE 4150*, 138-147, 2001.
- Bass, A. M. and R. J. Paur, The ultraviolet cross sections of ozone, I, measurements, in *Atmospheric Ozone, Proceedings of the Quadrennial Ozone Symposium, Halkidiki, Greece*, edited by X. Zeferos and A. Ghazi, pp. 606-616, D. Reidel, Hingham, Mass., 1985.
- Bates, D. R., Rayleigh by air, *Planet. Space. Sci.*, 32, 785-790, 1984.
- Bell, R.J., *Introductory Fourier Transform Spectroscopy*, Academic Press, 1972.
- Berk A., A., L. S. Bernstein and D.C. Robertson, MODTRAN: A moderate resolution model for LOWTRAN 7, AFGL-TR-89-0122, 42pp, 1989.
- Bucholtz, A., Rayleigh-scattering calculations for the terrestrial atmosphere, *App. Opt.*, 34, 2765-2773, 1995.
- Burrows, J. P. and K. V. Chance, SCIAMACHY and GOME: The scientific objectives, *Optical Method in Atmospheric Chemistry, SPIE1715*, 502-512, Berlin, F.R.G., 1992.
- Callies, J., E. Corpaccioli, M. Eisinger, A. Lefebvre, and A. Hahne, Ozone Monitoring by GOME-2 on the METOP satellites, *Proceedings of the Quadrennial Ozone Symposium*, 131-132, 2000.
- Camy-Peyret, C., P. Jeseck, T. Hawat, G. Durry, S. Payan, G. Berube, L. Rochette and D. Huguenin, The LPMA balloon-borne FTIR spectrometer for remote sensing of atmospheric constituents, *Proc. 12th ESA Symp. European Rocket and Balloon Programmes and Related Research*, 1995.
- Chance, K, and R. J. D. Spurr, Ring effect studies: Rayleigh scattering , including molecular parameters for rotational Raman scattering, and the Fraunhofer spectrum, *Appl. Opt.*, 36, 5224-5230, 1997
- Chance, K, J.P. Burrows, D. Perner, and W. Schneider, Satellite Measurements of Atmospheric Ozone Profiles,

- Including Tropospheric Ozone, from UV/Visible Measurements in the Nadir Geometry: A Potential Method to Retrieve Tropospheric Ozone, *J. Quant. Spectrosc. Radiat. Transfer*, 57, 467-476, 1997.
- Chance, K., Analysis of BrO Measurements from the Global Ozone Monitoring Experiment, *Geophys. Res. Lett.*, 17, 3335-3338, 1998.
- Chance, K. V., W. A. Traub, K. W. Jucks, and D. G. Johnson, On the use of O<sub>2</sub> spin-rotation lines for elevation angle calibration of atmospheric thermal emission spectra, *J. Infrared and Millimeter Waves*, 12, 581-588, 1991.
- Clarmann, T. v., G. Wetzel, H. Oelhaf, F. Friedl-Vallon, A. Linden, G. Maucher, M. Seefeldner, O. Trieschmann, and F. Lefevre, ClONO<sub>2</sub>, vertical profile and estimated mixing ratios of ClO and HOCl in winter Arctic stratosphere from Michelson interferometer for passive atmospheric sounding limb emission spectra, *J. Geophys. Res.*, 102, 16157-16168, 1997.
- Clough, S. A., F. X. Kneizys, E. P. Shettle, and G. P. Anderson, Atmospheric radiance and transmittance: FASCOD2, *Proc. 6<sup>th</sup> Conference on atmospheric radiation*, 141-144, 1986
- Clough, S. A., M. J. Iacono, and J. L. Moncet, Line-by-line calculations of atmospheric fluxes and cooling rates: Application to water vapor, *J. Geophys. Res.*, 97, 15761-15785, 1992.
- Clough, S. A. and M. J. Iacono, Line-by-line calculations of atmospheric fluxes and cooling rates 2: application to carbon dioxide, ozone, methane, nitrous oxide and the halocarbons, *J. Geophys. Res.*, 100, 16519-16535, 1995.
- Dave, J. V., Meaning of successive iteration of the auxiliary equation of radiative transfer, *Astrophys. J.*, 140, 1292-1303, 1964.
- Dessler, A. E., and P. Yang, The distribution of tropical thin cirrus clouds inferred from Terra MODIS data, *J. Climate*, 16, 1241-1247, 2003.
- Fisher, J., and H. Grassl, Detection of cloud-top height from backscattered radiances within the oxygen A band, 1, Theoretical study, *J. Appl. Meteorol.*, 30, 1245-1259, 1991.
- Fisher, J., W. Cordes, A. Schmitz-Peiffer, W. Renger and P. Morl, Detection of cloud-top height from backscattered radiances within the oxygen A band. Part 2: measurements, *J. Appl. Meteorol.*, 30, 1260-1267, 1991.
- Fleig, A. J., R. D. McPeters, P. K. Bhartia, B. M. Schlesinger, R. P. Cebula, K. F. Klenk, S. L. Taylor and D. F. Heath, Nimbus 7 Solar Backscatter Ultraviolet (SBUV) Ozone Products User's Guide, *NASA Ref. Publ.*, 1234, 128pp., 1990.
- Giver, L. P., R. W. Boese, and J. H. Miller, Intensity measurements, self-broadening coefficients, and rotational intensity distribution for lines of the Oxygen B band at 6880 Å, *J. Quant. Spectrosc. and Radiat. Transfer*, 14, 793-802, 1974.
- Gurney, K. R., R. M. Law, A. S. Denning, P. J. Raynor, D. Baker, P. Bousquet, L. Bruhwiler, Y-H Chen, P. Clais, S. Fan, I. Y. Fung, M. Gloor, M. Helmann, K. Higuchi, J. John, T. Maki, S. Maksyutov, K. Masario, P. Peylin, M. Prather, B. C. Pak, J. Randerson, J. Sarmiento, S. Taguchi, T. Takahashi, and C-W Yuon, Towards robust regional estimates of CO<sub>2</sub> sources and sinks using atmospheric transport models, *Nature*, 415, 626-630, 2002.

- Harrison, G. R., The production of diffraction grating: II. The design of echelle gratings and spectrographs, *J. Opt. Soc. Am.* 39, 522-528, 1949.
- Hasebe, F., M. Shiotani, T. Ogawa, S. Oltmans, K. Gage and H. Vomel, SOWER proposal, Workshop report, ESTO 97POA1-D007, 61pp, 1998.
- Heath, D. F., A. H. Krueger, H. A. Roeder and B. D. Henderson, The Solar Backscatter Ultraviolet and Total Ozone Mapping Spectrometer (SBUV/TOMS) for Nimbus G, *Opt. Eng.*, 14, 323-331, 1975.
- Heidinger, A., and G. L. Stephens, Molecular line absorption in a scattering atmosphere. Part II: Application to remote sensing in the O<sub>2</sub> A band, *J. Atom. Sci.*, 57, 1615-1634, 2000.
- Heney, L. C. and J. L. Greenstein, Diffuse radiation in the galaxy, *Astrophys. J.*, 93, 70-83 1941.
- Hobbs, P. V., Aerosol-Cloud-Climate Interactions edited by, Academic Press, 1993.
- Houze, R. A. Jr., Cloud Dynamics, Academic Press, 573 pp., 1993
- Hutley, M. C., Diffraction Gratings, *Academic Press*, 1990.
- The Intergovernmental Panel on Climate Change (IPCC) Third Assessment Report - Climate Change 2001 [available at <http://www.ipcc.ch/>].
- The International Satellite Cloud Climatology Project (ISCCP); cloud data and products [available at <http://isccp.giss.nasa.gov/products/onlineData.html>].
- Jacob, D. J., Introduction to Atmospheric Chemistry, University of Tokyo Press, 2002.
- Jointer, J., P. K. Bhartia, R. P. Cebula, E. Hilsenrath, R. D. McPeters, and H. Park, Rotational Raman scattering (Ring effect) in satellite backscatter ultraviolet measurements, *Appl. Opt.*, 34, 4513-4524, 1995.
- Kawashima, T., S. Mori, J. Tani, Y. Sasano, H. Nakajima, T. Yokota, T. Sugita, A. Kuze, and K. Waragai, Introduction of SOFIS/FTS calibration system, *SPIE 4818*, 193-200, 2002.
- Kerr, J. B., C. T. McElroy and R. A. Olafson, Measurements of ozone with the Brewer ozone spectrometer, Proceedings of Quadrennial International Ozone Symposium, Boulder, Colo., 74-79, 1980.
- Kimura, T., K. Kondo, H. Kumagai, H. Kuroiwa, Chu Ishida, R. Oki, A. Kuze, M. Suzuki, H. Okamoto, R. Imasu, T. Nakajima, EarthCARE-Earth clouds, aerosol and radiation explorer: it's objectives and Japanese sensor designs, *SPIE 4882-79*, 2002.
- Kneizys, F. X., E. P. Shettle, L. W. Abreu, J. H. Chetwynd, G. P. Anderson, W. O. Gallery, J. E. A. Selby, and S. A. Clough, Users guide to LOWTRAN 7, *AFGL Tech. Rep.*, 88-0177, 1-137, 1988.
- Kobayashi, H., IMG Project technical report, CRIEPI, 1999.
- Koелеmeijer, R. B. A., P. Stammes, J. W. Hovenier, and J. F. de Haan, A fast method for retrieval of cloud parameters using oxygen A band measurements from the Global Ozone Monitoring Experiment, *J. Geophys. Res.*, 106, 3475-3490, 2001.
- Koелеmeijer, R. B. A., P. Stammes, J. W. Hovenier, and J. F. De Haan, "Global distribution of effective cloud fraction and cloud top pressure derived from oxygen A band spectra measured by the Global Ozone Monitoring Experiment: comparison to ISCCP data," *J. Geophys. Res.* 107, 10.1029/2001JD000840 2002.
- Kramer, H. J., Observation of the earth and its environment, survey of missions and sensors, 3<sup>rd</sup> enlarged edition, Springer, 960 pp, 1996.
- Krueger, A. J., UV remote sensing of the earth's atmosphere, *Proceedings of the international school of physics*

- Enrico Fermi 124*, 155-181, 1995.
- Kurucz, R. L., and B. Bell, Atomic Line Data Kurucz CD-ROM No. 23, Cambridge, Mass. Smithsonian Astrophysical Observatory, 1995.
- Kuze, A. and K. V. Chance, Analysis of cloud top height and cloud coverage from satellites using O<sub>2</sub> A and B bands, *J. Geophys. Res.*, 99, 14481-14491, 1994.
- Kuze, A., M. Suzuki, and J. Tanii, High Radiance Cavity Blackbody System for Radiometric Calibration, 18th RESES Symposium Proceedings, 53-54, 1996.
- Kuze, A., M. Suzuki, K. Nakamura, J. Tanii and Y. Sasano, Design and performance of ILAS-II echelle grating spectrometer for ClONO<sub>2</sub> measurement, *SPIE 3437*, 240-248, 1998.
- Kuze, A., S. Sasaki, T. Sano and T. Ogawa, ADEOS TOMS Ozone Retrieval System developed at EORC, EORC Bulletin 1998, 38-54, 1998.
- Kuze, A., T. Kawashima, Y. Yamamoto, K. Shibasaki, M. Suzuki, T. Sano and T. Ogawa, Laboratory-model test results of Ozone Dynamics Ultraviolet Spectrometer (ODUS), Optical Remote Sensing of the Atmosphere, *OSA*, 1999.
- Kuze, A., H. Nakajima, J. Tanii, and Y. Sasano, Conceptual design of Solar Occultation FTS for Inclined-orbit Satellite (SOFIS) on GCOM-A1, *SPIE 4131*, 305-314, 2000.
- Kuze, A., T. Kawashima, K. Shibasaki, M. Suzuki, T. Sano, and T. Ogawa, Atmospheric composition measurement from ozone dynamics UV spectrometer (ODUS), *SPIE 4135*, 171-181, 2000.
- Kuze, A., T. Kawashima, Y. Yamamoto, K. Shibasaki, M. Suzuki, T. Sano, and T. Ogawa, Specifications of GCOM-A1/ODUS, *SPIE 4150*, 373-382, 2001.
- Kuze, A., H. Nakajima, M. Suzuki and Y. Sasano, Measurement of greenhouse gases from space with a SWIR FTS, *SPIE 4485*, 69-80, 2002.
- Kuze, A., H. Nakajima, J. Tanii, and Y. Sasano, Instrumentation and laboratory model test result of Solar Occultation FTS for Inclined-orbit Satellite (SOFIS) on GCOM-A1, *SPIE 4486*, 356-365, 2002.
- Laan, E., J. de Vries, B. Kruizinga, H. Visser, P. Levelt, G. H. J. van den Oord, A. Maelkki, G. Leppelmeier, and E. Hilsenrath, Ozone Monitoring with the OMI instrument, *SPIE 4132*, 334-343, 2000.
- Loewen, E., D. Maystre, E. Popov, and L. Tsonev, Echelles: scalar, electromagnetic, and real-groove properties", *Appl. Opt.*, 34, 1707-1727, 1995.
- Massie, V. T., J. A. Davidson, C. A. Cantrell, A. H. McDaniel, J. C. Gille, V. G. Kunde, J. C. Brasunas, B. J. Conrath, W. C. Maguire, A. Goldman, and M. M. Abbas, Atmospheric infrared emission of ClONO<sub>2</sub> observed by a balloon-borne Fourier spectrometer, *J. Geophys. Res.*, 92, 14806-14814, 1987.
- McGee, T. J. and Burris Jr., J., SO<sub>2</sub> absorption cross sections in the near U.V., *J. Quant. Spectrosc. Radiat. Transfer*, 37, 165-182, 1987.
- Miller, J. H., R. W. Boese, and L. P. Giver, Intensity measurements and rotational intensity distribution for the oxygen A band, *J. Quant. Spectrosc. and Radiat. Transfer*, 9, 1507-1517, 1969.
- Molina, L. T. and M. J. Molina, Absolute absorption cross section of ozone in the 185- to 350-nm wavelength range, *J. Geophys. Res.*, 91, 14501-14508, 1986.
- Nakajima T. and M. Tanaka, Algorithm for radiative intensity calculations in moderately thick atmospheres

- using a truncation approximation, *J. Quant. Spectrosc. Radiat. Transfer*, 40, 51-69, 1988.
- Nakajima, H., Solar Occultation FTS for Inclined-orbit Satellite (SOFIS), Global Change Observation Mission (GCOM)-A1 Workshop, Report on the GCOM-A1 Workshop, 95-112, Tokyo, 2000.
- Nakajima, H., A. Kuze, T. Sugita, T. Yokota, and Y. Sasano, Solar Occultation FTS for Inclined-orbit Satellite (SOFIS): Scientific requirements and current status of development," *SPIE 4150*, 165-173, 2001.
- Nicolet, M., On the molecular scattering in the terrestrial atmosphere: an empirical formula for its calculation in the homosphere, *Planet. Space. Sci.*, 32, 1467-1468, 1984.
- Ogawa H., M. Tanaka and T. Nakajima, A simple expression for the additional sky radiance produced by polarization effects, *J. Meteor. Soc. Japan*, 67, 877-888, 1989.
- Pak, B. C. and M. J. Prather, CO<sub>2</sub> source inversions using satellite observations of the upper troposphere, *Geophys. Res. Lett.*, 28, 4571-4574, 2001.
- Palmer, Z., and E. Loewen, Diffraction grating handbook, *Milton Roy Company*, 1993.
- Patterson E. M. , D. A. Gillette, and B. H. Stockton, L. T. and M. J. Molina, Complex index of refraction between 300 and 700 nm for Saharan aerosols, *J. Geophys. Res.*, 82, 3153-3160, 1977.
- Pitts, M. C., L. W. Thomason, and W. P. Chu, Satellite remote sensing of temperature and pressure by the Stratospheric Aerosol and Gas Experiment III, presented at the 9th Conference on Satellite Meteorology and Oceanography, Paris, France, May 1998.
- Planet, W. G., L. E. Flynn, E. Hilsenrath, J. Hornstein, E. Kang, J. Larsen, F. Sanner, C. Seftor, C. Wellemeier and G. Jaross, OMPS (Ozone Mapping and Profiling Suite): The next generation of United States operational ozone monitoring instruments, Proceedings of the Quadrennial Ozone Symposium, 589-590, 2000.
- Ramanathan V. and P. Crutzen, Concept on Atmospheric Brown Cloud project, United Nations Environment Programme, 2001 [available at <http://www-asianbrowncloud.ucsd.edu/>].
- Rinsland, Y. P., M. R. Gunson, M. C. Abrams, R. Zander, E. Mahieu, A. Goldman, M. K. W. Ko, J. M. Rodriguez, and N. D. Sze, Profiles of stratospheric chlorine nitrate (ClONO<sub>2</sub>) from atmospheric trace molecule spectroscopy/ATLAS 1 infrared solar occultation spectra, *J. Geophys. Res.*, 99, 18895-18900, 1994.
- Rodgers, C. D., Characterization and error analysis of profiles retrieved from remote sounding measurement, *J. Geophys. Res.*, 95, 5587-5595, 1990.
- Rodgers, C.D., Retrieval of atmospheric temperature and composition from remote measurements of thermal radiation, *Rev. Geophys. and Space Phys.*, 14, 609-624, 1976.
- Rodgers, C.D., The vertical resolution of remotely sounded temperature profiles with *a priori* statistics, *J. Atmos. Sci.*, 33, 707-709, 1976.
- Rothman, L. S., R. R. Gamache, A. Goldman, L. R. Brown, R. A. Toth, H. M. Pickett, R. L. Poynter, J.-M. Flaud, C. Camy-Peyret, A. Barbe, N. Husson, C. P. Rinsland, and M. A. H. Smith., The HITRAN database: 1986 edition, *Appl. Opt.*, 26, 4058-4097, 1987.
- Rothman, L., R. R. Gamache, R. H. Tipping, C. P. Rinsland, M. A. H. Smith, D. C. Benner, V. M. Devi, J.-M. Flaud, C. Camy-Peyret, A. Perrin, A. Goldman, S. T. Massie, L. R. Brown, and R. A. Toth, The HITRAN molecular database: Editions of 1991 and 1992, *J. Quant. Spect. Radiat. Transfer*, 48, 469-508, 1992.

- Rothman, L. S., C. P. Rinsland, A. Goldman, S.T. Massie, D. P. Edwards, J.-M. Flaud, A. Perrin, C. Camy-Peyret, V. Dana, J.-Y. Mandin, J. Schroeder, A. McCann, R.R. Gamache, R. B. Wattson, K. Yoshino, K. V. Chance, K. W. Jucks, L. R. Brown, V. Nemtchinov, and P. Varanasi, The HITRAN Molecular Spectroscopic Database and HAWKS (HITRAN Atmospheric Workstation): 1996 Edition, *Quant. Spectrosc. and Radiat. Transfer*, 60, 665-710, 1998.
- Saiedy, F., H. Jacobowitz and D. Q. Wark, On cloud-top determination from Gemini-5, *J. Atmos. Sci.*, 24, 63-69, 1967.
- Sasano Y., M. Suzuki, T. Yokota, and H. Kanzawa, Improved Limb Atmospheric Spectrometer (ILAS) for stratospheric ozone layer measurements by solar occultation technique, *Geophys. Res. Lett.*, 26, 197-200, 1999.
- Sasano, Y., and O. Mizuno, ILAS-III (Solar Occultation FTS) project, *8th International Workshop on Atmospheric Science from Space using Fourier Transform Spectrometry*, 43-46, 1999.
- Scott A., B. Mackay, S. Wang, N. Rowlands, G. Shepherd, W. Gault, I. McDade, and Y. J. Rochon, The SWIFT instrument, *SPIE 4150*, 420-426, 2001.
- Smith, W. L., and C. M. R. Platt, Comparison of satellite-deduced cloud heights with indications from radiosonde and ground-based laser measurements, *J. Appl. Meteorol.*, 17, 1796-1802, 1978.
- Solomon, S., R. R. Garcia, F. S. Rowland, and D. J. Wuebbles, On the depletion of Antarctic ozone, *Nature*, 321, 755-758, 1986.
- Spurr, R. J. D., T. P. Kurosu, and K. V. Chance, A linearized discrete ordinate radiative transfer model for atmospheric remote sensing retrieval, *J. Quant. Spectrosc. Radiant. Transfer*, 68, 689-735, 2001.
- Stephens, G. L., and A. Heidinger, Molecular line absorption in a scattering atmosphere. Part I: Theory, *J. Atom. Sci.*, 57, 1599-1614, 2000.
- Sugita, T., T. Yokota, T. Nakajima, H. Nakajima, K. Waragai, M. Suzuki, A. Matsuzaki, Y. Itou, H. Saeki, and Y. Sasano, Temperature and pressure retrievals from O<sub>2</sub> A-band absorption measurements made by ILAS: Retrieval algorithm and error analysis, *SPIE4150*, 94-105, 2000.
- Suzuki, K., T. Ogawa and S. Kadokura, The UV experiment for the satellite "OHZORA", *ISAS report*, 12, 1985.
- Suzuki, M., Y. Sasano, T. Ishigaki, N. Kimura, N. Araki, A. Matsuzaki, Improved limb atmospheric spectrometer, ILAS, *SPIE 2268*, 103-110, 1994.
- Suzuki, M., Y. Sasano, T. Ishigaki, N. Kimura, N. Araki, K. Nakamura, A. Kuze, and J. Tanii, Conceptual design study of ILAS-II onboard ADEOS-II, *SPIE 2553*, 48-55, 1995.
- Suzuki, M., K. Shibasaki, H. Shimoda, and T. Ogawa, Overview of science program of GCOM-A1 satellite, *SPIE 4135*, 150-159, 2000.
- Thompson, A.M., J.C. Witte, R.D. McPeters, S. J. Oltmans, F. J. Schmidlin, J. A. Logan, M. Fujiwara, V. W. J. H. Kirchhoff, F. Posny, G. J. R. Coetzee, B. Hoegger, S. Kawakami, T. Ogawa, B. J. Johnson, H. Vömel and G. Labow, Southern Hemisphere Additional Ozonesondes (SHADOZ) 1998-2000 tropical ozone climatology 1. Comparison with Total Ozone Mapping Spectrometer (TOMS) and ground-based measurements, *J. Geophys. Res.*, 108, 8238, 10.1029/2001JD000967, 2003.

- Thompson, A.M., J.C. Witte, S. J. Oltmans, F. J. Schmidlin, J. A. Logan, M. Fujiwara, V. W. J. H. Kirchhoff, F. Posny, G. J. R. Coetzee, B. Hoegger, S. Kawakami, T. Ogawa, J. P. F. Fortuin, and H. M. Kelder, Southern Hemisphere Additional Ozonesondes (SHADOZ) 1998-2000 tropical ozone climatology 2. Tropospheric variability and the zonal wave-one, *J. Geophys. Res.*, *108*, 8241, 10.1029/2002JD002241, 2003.
- Torres, O., P. K. Bhartia, J. R. Herman, Z. Ahmad, and J. Gleason, Deviation of aerosol properties from satellite measurements of backscattered ultraviolet radiation: Theoretical basis, *J. Geophys. Res.*, *103*, 17,099-17,110, 1998.
- Torres, O., P. K. Bhartia, J. R. Herman, Z. Sinyuk, P. Ginoux, and B. Holman, A long term record of aerosol optical depth from TOMS observations and comparison to AERONET measurements, *J. Atmos. Sci.*, *59*, 398-413, 2002.
- Total Ozone Mapping Spectrometer, Nimbus-7 TOMS Data & Images, 2002 [available at <http://toms.gsfc.nasa.gov/n7toms/nim7toms.html>].
- Twomey, S., Introduction to the mathematics of inversion in remote sensing and indirect measurements, Elsevier Scientific Publishing Company, 1977.
- Uemura N., T. Yokota, H. Nakajima, T. Sugita, Y. Sasano, C. Yoshigahara, and Y. Uehara, A preliminary study on data processing algorithms for SOFIS, *SPIE 4150*, 174-187, 2001.
- USGS spectral library [available at <ftp://speclab.cr.usgs.gov/pub/spectral.library/spectral-lib.desc+plots.html>].
- Wark, D. G., and D. M. Mercer, Absorption in the atmosphere by the oxygen "A" Band, *Appl. Opt.*, *4*, 839-844, 1965.
- Webster, C. R., R. D. May, D. W. Toohey, L. M. Avallone, J. G. Anderson, P. Newman, L. Lait, M. R. Shoeberl, J. W. Elkins, and K. R. Chan, "Chlorine chemistry on polar stratospheric cloud particles in the Arctic winter", *Science*, *261*, 1130-1134, 1993.
- Wellemeyer, C., C. Seftor, G. Jaross, and P. K. Bhartia, Evaluation of errors in the version 7 TOMS algorithm, Proceedings of the Quadrennial Ozone Symposium, 719-720, 2000.
- Yamamoto, G., and D. Q. Wark, Discussion of the letter by R. A. Hanel, determination of cloud altitude from a satellite, *J. Geophys. Res.*, *66*, 3596, 1961.
- Yamamoto, Y., A. Kuze, T. Kawashima, K. Shibasaki, M. Suzuki, T. Sano, and T. Ogawa, Ozone Dynamics Ultraviolet Spectrometer (ODUS), *SPIE 3756*, 25-33, 1999.
- Yamamoto, Y., A. Kuze, T. Kawashima, K. Shibasaki, M. Suzuki, T. Sano, and T. Ogawa, Conceptual design of the Ozone Dynamics Ultraviolet Spectrometer (ODUS) on the Global Change Observation Mission (GCOM) –A1 satellite, *SPIE 4135*, 160-170, 2000.